

1 **Scale dependence of earthquake rupture prestress in**
2 **models with enhanced weakening: implications for**
3 **event statistics and inferences of fault stress**

4 **Valère Lambert¹ Nadia Lapusta^{1,2} Daniel Faulkner³**

5 ¹Seismological Laboratory, California Institute of Technology, Pasadena, California, USA

6 ²Department of Mechanical and Civil Engineering, California Institute of Technology, Pasadena,
7 California, USA

8 ³School of Environmental Sciences, University of Liverpool, Liverpool, UK

9 **Key Points:**

- 10 • Local shear prestress varies significantly within and among ruptures, being close
11 to the quasi-static fault strength in nucleation regions.
- 12 • Efficient weakening allows rupture propagation over areas of lower prestress, lead-
13 ing to lower average prestress over larger rupture areas.
- 14 • Fault models with more efficient dynamic weakening produce fewer smaller events
15 and result in systematically lower b-values.

Corresponding author: Valère Lambert, vlambert@caltech.edu

16 **Abstract**

17 Determining conditions for earthquake slip on faults is a key goal of fault mechanics highly
18 relevant to seismic hazard. Previous studies have demonstrated that enhanced dynamic
19 weakening (EDW) can lead to dynamic rupture of faults with much lower shear stress
20 than required for rupture nucleation. We study the stress conditions before earthquake
21 ruptures of different sizes that spontaneously evolve in numerical simulations of earth-
22 quake sequences on rate-and-state faults with EDW due to thermal pressurization of pore
23 fluids. We find that average shear stress right before dynamic rupture (aka shear pre-
24 stress) systematically varies with the rupture size. The smallest ruptures have prestress
25 comparable to the local shear stress required for nucleation. Larger ruptures weaken the
26 fault more, propagate over increasingly under-stressed areas due to dynamic stress con-
27 centration, and result in progressively lower average prestress over the entire rupture.
28 The effect is more significant in fault models with more efficient EDW. We find that, as
29 a result, fault models with more efficient weakening produce fewer small events and re-
30 sult in systematically lower b-values of the frequency-magnitude event distributions. The
31 findings 1) illustrate that large earthquakes can occur on faults that appear not to be
32 critically stressed compared to stresses required for slip nucleation; 2) highlight the im-
33 portance of finite-fault modeling in relating the local friction behavior determined in the
34 lab to the field scale; and 3) suggest that paucity of small events or seismic quiescence
35 may be the observational indication of mature faults that operate under low shear stress
36 due to EDW.

37 **1 Introduction**

38 Determining the absolute level and controlling factors of the stress state on faults
39 has profound implications for earthquake physics, seismic hazard assessment, and the
40 role of faulting in plate tectonics and geodynamics. Numerous lines of field evidence sug-
41 gest that the average shear stress acting on mature faults must be low, 20 MPa or less,
42 in comparison to the expected shear resistance of 100 - 200 MPa averaged over the seis-

43 mogenic depth, given rock overburden and hydrostatic pore fluid pressure, along with
44 typical quasi-static friction coefficients of 0.6 - 0.85 (aka "Byerlee friction") measured
45 in laboratory experiments (Brune et al., 1969; Henyey & Wasserburg, 1971; Sibson, 1975;
46 Byerlee, 1978; Lachenbruch & Sass, 1980; Townend & Zoback, 2004; Rice, 2006; Suppe,
47 2007; Tanikawa & Shimamoto, 2009; Nankali, 2011; Fulton et al., 2013; Gao & Wang,
48 2014). Such evidence includes the lack of a substantial heat flow anomaly around ma-
49 ture faults that would be expected for fault slip at 100 MPa or more (Brune et al., 1969;
50 Henyey & Wasserburg, 1971; Lachenbruch & Sass, 1980; Nankali, 2011; Gao & Wang,
51 2014), inferences of steep angles between the principal stress direction and fault plane
52 (Townend & Zoback, 2004), analyses of the fault core obtained by drilling through shal-
53 low parts of faults that have experienced major recent events, including the 2011 M_w
54 9.0 Tohoku-oki event (Tanikawa & Shimamoto, 2009; Fulton et al., 2013), the geome-
55 try of thrust-belt wedges (Suppe, 2007), and the existence of long-lived narrow shear zones
56 that do not exhibit any evidence of melting (Sibson, 1975; Rice, 2006). Note that such
57 evidence for apparent fault weakness pertains predominantly to mature faults, whereas
58 some studies suggest that smaller, less mature faults may sustain the expected high shear
59 stresses given Byerlee friction values and overburden minus hydrostatic pore pressure (e.g.
60 Townend & Zoback, 2000).

61 A relatively straightforward explanation for the low-stress operation of mature faults
62 is that they may be persistently weak (Figure 1), due to the presence of anomalously low
63 quasi-static friction coefficients and/or low effective normal stress from pervasive fluid
64 overpressure (Brown et al., 2003; Faulkner et al., 2006; Bangs et al., 2009; Collettini et
65 al., 2009; Lockner et al., 2011). However, most materials with low quasi-static friction
66 coefficients (less than 0.5) under laboratory conditions tend to exhibit velocity-strengthening
67 behavior (Ikari et al., 2011), which would preclude spontaneous nucleation of dynamic
68 ruptures. Moreover, while evidence of substantial fluid overpressure has been documented
69 for many subduction zones (Brown et al., 2003; Bangs et al., 2009), there remains much
70 debate over the ubiquity of chronic near-lithostatic fluid overpressurization along faults

71 in other tectonic settings, such as continental faults, with some borehole measurements
72 suggesting fluid pressure levels more consistent with hydrostatic conditions (Townend
73 & Zoback, 2000; Zoback et al., 2010).

74 An alternative hypothesis for explaining such low-stress, low-heat operation is that
75 mature faults are indeed strong at slow, quasi-static sliding rates but undergo consid-
76 erable enhanced dynamic weakening at seismic slip rates, which has been widely hypoth-
77 esized in theoretical studies and documented in laboratory experiments (Figure 1, dashed
78 black line; Sibson, 1973; Tsutsumi & Shimamoto, 1997; Rice, 2006; Wibberley et al., 2008;
79 Di Toro et al., 2011; Noda et al., 2009; Acosta et al., 2018). The presence of enhanced
80 dynamic weakening on natural faults has been questioned by the expectation that en-
81 hanced dynamic weakening would produce much larger static stress drops than typical
82 values of 1 to 10 MPa inferred from earthquakes on natural faults (Allmann & Shearer,
83 2009; Ye et al., 2016b). The expectation is based on a common assumption that the shear
84 prestress over the entire rupture area should be near the static strength of the fault while
85 the final shear stress should be near the dynamic strength of the fault, resulting in a large
86 static stress change. However, a number of numerical and laboratory studies have demon-
87 strated that, once nucleated, dynamic ruptures can propagate under regions with pre-
88 stress conditions that are well below the expected static strength, based on prescribed
89 or measured quasi-static friction coefficients and confining conditions (Zheng & Rice, 1998;
90 Noda et al., 2009; Lu et al., 2010; Dunham et al., 2011; Gabriel et al., 2012; Fineberg
91 & Bouchbinder, 2015) while the final shear stress could be higher than dynamic shear
92 stress for pulse-like ruptures, with both inferences promoting reasonable stress drops. Such
93 studies have often considered a single dynamic rupture nucleated artificially and prop-
94 agating over uniform prestress conditions.

95 Recent numerical studies of earthquake sequences have shown that fault models
96 with a combination of both hypotheses for low-stress operation, including some chronic
97 fluid overpressure as well as mild-to-moderate enhanced dynamic weakening due to the

98 thermal pressurization of pore fluids, work well for reproducing a range of observations
99 (Perry et al., 2020; Lambert et al., in press). These include reasonable static stress drops
100 between 1 - 10 MPa nearly independent of earthquake magnitude, the seismologically
101 inferred increase in average breakdown energy with rupture size, the radiation ratios be-
102 tween 0.1 and 1 inferred for natural events, and the heat flow constraints. The simula-
103 tions produce mainly crack-like or mild pulse-like ruptures, with no significant under-
104 shoot. The near magnitude-invariance of average static stress drop arises in these fault
105 models because enhanced dynamic weakening results in both lower average prestress and
106 lower average final shear stress for larger ruptures with larger slip, with the average static
107 stress drops being nearly magnitude-independent. These studies suggest that distinguish-
108 ing between the conditions required for rupture nucleation and propagation is important
109 for assessing the relationship between laboratory friction measurements, seismological
110 observations and the absolute stress conditions on faults.

111 Here, we use and expand upon the set of numerical models from Perry et al. (2020)
112 and Lambert et al. (in press) to document the variability of prestress on a fault that arises
113 from the history of previous ruptures, and to study the relation between the size of dy-
114 namic rupture events and the average shear prestress over the rupture area. We also ex-
115 amine how the complexity of earthquake sequences, in terms of the variability of rup-
116 ture size, differs with the efficiency of dynamic weakening. We study these behaviors in
117 the context of simulations of sequences of earthquakes and slow slip, which allow the pre-
118 stress conditions before earthquakes to be set by the loading conditions, evolving fault
119 shear resistance (including weakening and healing), and stress redistribution by prior slip,
120 as would occur on natural faults. Moreover, our simulations resolve the spontaneous nu-
121 cleation process with the natural acceleration of slow unsteady slip prior to dynamic rup-
122 ture. The constitutive relations for the evolving fault resistance and healing adopted in
123 our models have been formulated as a result of a large body of laboratory, field and the-
124 oretical work (e.g Sibson, 1973; Dieterich, 1979; Ruina, 1983; Rice, 2006; Wibberley et
125 al., 2008; Di Toro et al., 2011). Indeed, laboratory experiments of fault shear resistance

126 at both slow and fast slip rates have been indispensable for our understanding of fault
127 behavior and for formulating fault models such as the ones used in this study. The mod-
128 elling allows us to examine the implications of the laboratory-derived constitutive be-
129 haviors for the larger-scale behavior of faults, and we compare our inferences of average
130 shear prestress from relatively large-scale finite-fault modeling to field measurements of
131 crustal stresses acting on mature faults and small-scale laboratory measurements of the
132 shear resistance of typical fault materials.

133 **2 Building on laboratory constraints to model larger-scale fault be-** 134 **havior**

135 Laboratory experiments have been instrumental for exploring aspects of fault re-
136 sistance during both slow and fast sliding (10^{-9} m/s - 1 m/s, Figure 1). Experiments
137 with slow sliding velocities ($< 10^{-3}$ m/s) are critical for formulating fault constitutive
138 laws that form the basis for understanding the nucleation of earthquake ruptures. High-
139 velocity laboratory friction experiments have demonstrated enhanced dynamic weaken-
140 ing of faults and elucidated a range of mechanisms by which this dynamic weakening can
141 occur (e.g. Han et al., 2007; Wibberley et al., 2008; Goldsby & Tullis, 2011; Di Toro et
142 al., 2011; Faulkner et al., 2011; De Paola et al., 2015; Acosta et al., 2018). Most slow-
143 and high-velocity experiments measure or infer the relevant quantities - slip, slip rate,
144 shear stress etc - averaged over the sample and examine the evolution of shear resistance
145 corresponding to a particular history of loading, such as imposed variations in the dis-
146 placement rate of the loading piston, and the particular fault conditions (normal stress,
147 temperature, pore fluid pressure, etc.). Some experimental studies imposed the expected
148 sliding motion during earthquakes in order to directly relate laboratory stress measure-
149 ments to seismological quantities, such as static stress drop and breakdown energy (e.g.
150 Sone & Shimamoto, 2009; Fukuyama & Mizoguchi, 2010; Nielsen et al., 2016).

151 To understand the full implications of the evolution of shear resistance measured
 152 in small-scale experiments for slip at larger scales along natural faults, they are synthe-
 153 sized into mathematical formulations and used in numerical modeling, for the following
 154 reasons. During slipping events on a finite fault over scales of tens of meters to kilome-
 155 tres - much larger than the experimental scale - the fault does not slip uniformly with
 156 a predetermined slip-rate history. Rather, the slip event initiates on a portion of the fault
 157 and then spreads along the fault, with varying slip-rate histories and final slips at dif-
 158 ferent points along the fault. This is captured in inversions of large earthquakes (e.g. Heaton,
 159 1990; Simons et al., 2011; Ye et al., 2016a; Tinti et al., 2016) and, to a degree, in larger-
 160 scale experiments, sometimes involving analog materials (Lu et al., 2010; McLaskey et
 161 al., 2014; Svetlizky & Fineberg, 2014; Yamashita et al., 2015; Rubino et al., 2017). In
 162 the process, the slip (1) transfers stress to the more locked portions of the fault and (2)
 163 enters portions of the fault with different conditions - such as levels of shear pre-stress,
 164 pore fluid pressure, etc - and potentially different friction and hydraulic properties. Hence
 165 the resulting coupled evolution of shear resistance and slip rate at different locations on
 166 the fault is often quite different and, through stress transfer, strongly dependent on the
 167 entire slip process at all locations throughout the rupture. These nonlinear and often dy-
 168 namic feedback processes on the scales of tens of meters to kilometers can currently be
 169 only captured through numerical modeling.

170 Many numerical models of earthquake source processes utilize insight from labo-
 171 ratory experiments that indicate that the resistance to shear τ along a fault depends on
 172 the sliding rate V and the quality and/or lifetime of the local contacts, typically param-
 173 eterized by a state variable θ with units of time, as well as on the effective normal stress
 174 $\bar{\sigma} = \sigma - p$ acting on the fault, with σ being the normal stress and p being the pore fluid
 175 pressure localized within the shearing layer (e.g. Dieterich, 1979; Marone, 1998). For con-
 176 tinuum problems involving frictional sliding, the motion within the continuum is gov-
 177 erned by the balance of linear momentum, subject to the boundary condition that trac-
 178 tions are given by the constitutive law of the interface. For frictional sliding without changes

179 in the elastodynamic normal stress, which is the case considered in this work, the bound-
 180 ary condition reduces to the shear stress being equal to the shear resistance on the in-
 181 terface ($y = 0$):

$$\begin{aligned}\tau_{\text{stress}}(x, y = 0, z; t) &= \tau_{\text{resistance}}(x, y = 0, z; t) \\ &= f(V, \theta)(\sigma - p).\end{aligned}\tag{1}$$

182 An important concept in the rate-and-state formulation of the friction coefficient $f(V, \theta)$
 183 is that the friction coefficient is not a fixed property of the interface but evolves over time,
 184 facilitating the time-dependent changes of shear resistance and hence shear stress along
 185 the fault during shear.

186 The most commonly used formulation of rate-and-state laws is the Dieterich-Ruina
 187 formulation (Dieterich, 1979; Ruina, 1983):

$$f(V, \theta) = \left[f_* + a \ln \frac{V}{V_*} + b \ln \frac{\theta V_*}{L} \right],\tag{2}$$

188 where f_* is a reference steady-state friction coefficient at the reference sliding rate V_* ,
 189 L is the characteristic slip distance, and a and b are the direct effect and evolution ef-
 190 fect parameters, respectively. Our fault models are governed by a form of the laboratory-
 191 derived Dieterich-Ruina rate-and-state friction law regularized for zero and negative slip
 192 rates (Lapusta et al., 2000; Noda & Lapusta, 2010). The evolution of the state variable
 193 can be described by various evolution laws; we employ the aging law (Ruina, 1983):

$$\dot{\theta} = 1 - \frac{V\theta}{L},\tag{3}$$

194 which describes evolution during sliding as well as time-dependent healing in near-stationary
195 contact. In our models, the shear resistance and shear stress also change due to the evo-
196 lution of pore fluid pressure p .

197 We conduct numerical simulations following the methodological developments of
198 Lapusta et al. (2000), Noda and Lapusta (2010) and Lambert et al. (in press) in order
199 to solve the elastodynamic equations of motion with the fault boundary conditions, in-
200 cluding the evolution of pore fluid pressure and temperature on the fault coupled with
201 off-fault diffusion. The simulations solve for mode III slip on a 1-D fault embedded into
202 a 2-D uniform, isotropic, elastic medium (Figure 2). The potential types of slip on the
203 fault include sequences of earthquakes and aseismic slip (SEAS) and they are simulated
204 in their entirety, including the nucleation process, dynamic rupture propagation, post-
205 seismic slip that follows the event, and interseismic period between seismic events that
206 can last up to tens or hundreds of years and host steady and transient slow slip (Fig-
207 ure 2).

208 The simulated fault in our models contains a 24-km-long segment with velocity-
209 weakening (VW) frictional properties where earthquake ruptures may nucleate and prop-
210 agate, surrounded by velocity-strengthening (VS) segments that inhibit rupture nucle-
211 ation and propagation. Our simulations include enhanced dynamic weakening due to the
212 thermal pressurization of pore fluids, which occurs when pore fluids within the fault shear-
213 ing layer heat up and pressurize during dynamic rupture, reducing the effective normal
214 stress and shear resistance (Sibson, 1973; Rice, 2006; Noda & Lapusta, 2010). Thermal
215 pressurization is one potential mechanism for enhanced weakening; qualitatively simi-
216 lar results should hold for models with other types of enhanced dynamic weakening. We
217 follow the thermal pressurization formulation of Noda and Lapusta (2010) (Supplemen-
218 tary Materials).

219 For the purpose of comparing local frictional behavior with the average prestress
220 for dynamic ruptures of varying sizes, we focus this study on simulated ruptures that ar-

rest within the VW region, where the friction properties are uniform with a quasi-static reference friction of 0.6, consistent with many materials exhibiting VW behavior in laboratory experiments (Ikari et al., 2011). We examine the evolution of the apparent friction coefficient, or the ratio of the current shear stress τ to the interseismic drained effective normal stress ($\sigma - p_{\text{int}}$), where p_{int} is the interseismic drained value of the pore pressure. The "drained" refers to the effective stress with ambient pore pressure unaffected by slip processes such as dilatancy, compaction, or thermal pressurization.

We examine fault models with varying levels of ambient fluid overpressure in terms of the effective normal stress, as well as varying degrees of efficiency in enhanced weakening due to thermal pressurization. The parameter values we have chosen (Tables 1-3) are motivated by prior studies that have reproduced a range of seismological observations as well as low-stress, low-heat operation of mature faults (Perry et al., 2020; Lambert et al., in press). The parameter values also facilitate our goal of examining ruptures in fault models with a range of efficiency in enhanced dynamic weakening. We define the beginning and end of dynamic rupture, t_{ini} and t_{fin} respectively, as well as the ruptured area Ω , using a slip velocity threshold ($V_{\text{thresh}} = 0.01$ m/s) for seismic slip, based on previous studies (Perry et al., 2020; Lambert et al., in press). Note that t_{ini} and t_{fin} refer to the beginning and end of the entire rupture event, which starts when one location on the fault reaches the threshold velocity and ends when all points on the fault drop below the threshold velocity. In the following, we use "rupture" to refer to such dynamic slip events, unless noted otherwise. Further description of the numerical methodology can be found in the Supplementary Materials.

3 Evolution of local slip and shear resistance and notions of failure

Our simulations capture the evolution of motion and shear stress across the fault over sequences of earthquakes spanning several thousands of years (Figure 2C). The initial distributions of shear stress and other quantities such as the slip rate are assumed

247 to be uniform along most of the VW region of the fault at the start of our simulations,
 248 other than a small region of initially high prestress near the VW-VS boundary to nu-
 249 cleate the first rupture in the earthquake sequence. The distributions of shear stress and
 250 slip along the fault evolve to become highly variable throughout periods of fast earthquake-
 251 producing slip as well as slow aseismic slip and fault locking. Below we review how the
 252 rate-and-state friction framework allows the model to represent both creeping, locked,
 253 and seismically slipping fault areas as well as transitions between these different styles
 254 of slip.

255 During dynamic rupture, the evolution of slip rate and shear stress can be partic-
 256 ularly complex and variable along the fault. At points where individual ruptures nucle-
 257 ate, the slip rate gradually accelerates towards seismic slip rates and shear stress at the
 258 beginning of rupture, t_{ini} , is relatively high, with the apparent friction coefficient $\tau/(\sigma -$
 259 $p_{\text{int}})$ close to the quasi-static reference friction of 0.6. As seismic slip rates are reached,
 260 $\tau/(\sigma - p_{\text{int}})$ drops substantially due to thermal pressurization of pore fluids in a man-
 261 ner qualitatively consistent with the enhanced dynamic weakening observed in high-velocity
 262 laboratory friction experiments (Figure 2H). The evolution of slip rate and shear stress
 263 outside of the nucleation region is even more complicated: The shear stress at t_{ini} , prior
 264 to the arrival of the rupture front, can be much lower than the shear stress levels where
 265 the rupture nucleates, then increases to a higher peak shear stress that reflects the in-
 266 terseismic fault healing and rate-and-state direct effect and is achieved due to the dy-
 267 namic stress concentration at the rupture front, and then decreases due to weakening
 268 with seismic slip (Figure 2H vs. I). Consistently, the slip rate rapidly increases to seis-
 269 mic values at the beginning of slip and then decreases, as in a typical Yoffe-like behav-
 270 ior for dynamic ruptures (Figure 2G; e.g Tinti et al., 2005). Thus, even with the uni-
 271 form normal stress and uniform parameters of the assumed friction and pore pressure
 272 equations within the seismogenic VW region, the prestress conditions throughout the
 273 rupture area can be highly variable and, in part, substantially different between regions
 274 of rupture nucleation and rupture propagation.

275 Note that the peak shear stress during dynamic rupture of fault locations outside
 276 the nucleation zone can correspond to much higher apparent friction coefficient (e.g., 0.95
 277 in Figure 2I) than the reference friction coefficient ($f_* = 0.6$ in this study). This is due
 278 to both the direct effect at the rupture tip and the high, interseismically "healed" value
 279 of the state variable θ , as discussed in Lambert and Lapusta (2020) and the Supplemen-
 280 tary Materials (equation S3). As follows from the first line of equation S3, the difference
 281 between the peak friction coefficient and f_* due to the direct effect of $a \ln(V_{\text{peak}}/V_*)$ would
 282 be 0.14 to 0.16 for $V_{\text{peak}} = 1$ to 10 m/s and other parameters of our model, with the
 283 rest due to the much larger value of the "healed" state variable than that for sliding at
 284 the reference sliding rate.

285 The local evolution of shear stress throughout the VW seismogenic zone differs among
 286 points based on the long-term history of motion, including both local slip as well as slip
 287 across the entire fault. For example, a point at the center of the VW region ($z = 0$ km)
 288 of one of our simulations (fault model TP 3 in Table 2, as shown in Figure 2C) experi-
 289 ences substantial slip only during the largest earthquake ruptures that span the entire
 290 VW domain, resulting in a relatively simple and quasi-repetitive pattern of stress accu-
 291 mulation and weakening over sequences of earthquakes (Figure 3A & C). In contrast, an-
 292 other point in the VW region closer to the VS boundary ($z = -9.6$ km) experiences dif-
 293 ferent amounts of slip during dynamic ruptures of varying size, resulting in a more com-
 294 plicated evolution of shear stress with accumulating slip (Figure 3B & D).

295 In between individual earthquakes, the VS regions of the fault creep (i.e., slowly
 296 slip) with the slip rate close to the prescribed tectonic plate rate, due to that rate be-
 297 ing imposed on the fault areas nearby, with occasional quasi-static accelerations due to
 298 post-seismic slip (Figure 4, left column). The creep penetrates into the VW regions nearby,
 299 creating fault areas prone to earthquake nucleation (Jiang & Lapusta, 2016; Michel et
 300 al., 2017) (Figure 4, right column). These points of the VW region close to the VS re-
 301 gion (within one or so nucleation length) are reloaded due to creep and post-seismic slip

302 from previous rupture within the VS regions. The loading rate at these points near the
303 VS-VW boundary varies over time depending on the rate of motion in the VS region,
304 which in turn depends on the previous history of co-seismic slip during dynamic ruptures
305 in the VW region.

306 The slip rate and apparent friction at points close to the VW-VS boundary are typ-
307 ically brought to near steady conditions around the loading plate rate, however both ex-
308 hibit small oscillations as these points continue to be loaded by creep in the VS region,
309 resulting in further acceleration, slip and weakening, and thus the transmission of stress
310 further into the VW region until a sufficiently large area is loaded to sustain rupture nu-
311 cleation and acceleration to seismic slip rates (Figure 4E-G). This oscillatory behavior
312 is consistent with predictions from the stability analysis of a single degree-of-freedom spring-
313 slider undergoing frictional slip, where the amplitude of the oscillations is expected to
314 grow as the spring stiffness decreases below a critical stiffness value until (Gu et al., 1984).
315 The effective stiffness of the slipping fault zone in a continuum model is inversely pro-
316 portional to the slipping zone size (Rice & Ruina, 1983), decreasing with the increas-
317 ing slipping region. Note that this rate-and-state nucleation process has been used to
318 explain the period-dependent response of microseismicity to periodic stress perturbations
319 in Nepal, where seismicity shows significant variations in response to annual monsoon-
320 induced stress variations but not to semidiurnal tidal stresses of the same magnitude (Ader
321 et al., 2014).

322 In contrast, much of the VW region further away from the VS regions is essentially
323 locked, which is expressed in the rate-and-state formulation as sliding at very low, but
324 still non-zero, slip rates that are many orders of magnitude smaller than the loading rate
325 (Figure 5A-B). This differential motion between the VS and VW regions loads points
326 in the VW region (Figure 5C-D), gradually increasing shear stress there (e.g., between
327 700 and 800 years in Figure 5C). Note that the interseismic stressing rate is higher at
328 locations closer to the creeping regions than further away from it (Figures 5C vs. 5D vs.

329 4F), as one would expect. At the same time, the essentially locked points within the VW
 330 region experience time-dependent healing of the local shear resistance encapsulated in
 331 the increase of the state variable θ (Figure 5E-F). One of the manifestations of this heal-
 332 ing is that larger interseismic increases in the state variable generally lead to higher peak
 333 shear stress during dynamic rupture propagation (Lambert & Lapusta, 2020). Despite
 334 the increase in the state variable, its value is far below the steady-state one for the very
 335 low interseismic slip rates, consistent with continuing healing prior to dynamic rupture
 336 (Figure 5G-H). Depending on whether the local shear stressing rate (which increases the
 337 shear stress τ on the left of equation 1) is larger or smaller than the rate of healing (ex-
 338 pressed by the last, θ term on the right hand side of equation 2), the local slip rate (that
 339 enters the second term of equation 2) increases (as between 700 and 800 years in Fig-
 340 ure 5A) or decreases, i.e., the fault is accelerating towards failure or becomes even more
 341 locked. However, most of the locked points of the fault never accelerate close to failure
 342 interseismically; rather, they fail due to stress concentrations from dynamic events, seen
 343 as vertical lines in Figure 5C-D.

344 We note that healing on natural faults, in the presence of fluids and depth-dependent
 345 elevated temperatures, can be affected by a number of mechanisms that are not captured
 346 by the basic state evolution equation (Yasuhara et al., 2005; Tenthorey & Cox, 2006; Chen
 347 et al., 2015a, 2015b). Incorporating more realistic healing into shear resistance formu-
 348 lations and numerical modelling is an important goal for future work. This can be done
 349 by modifying the evolution of the state variable θ or adding other state variables that
 350 would encode healing. Yet, qualitatively, additional healing mechanisms would have sim-
 351 ilar effects on the simulations as the current rate-and-state healing, in that the healing
 352 would modify the peak shear resistance and the subsequent evolution of the resistance
 353 based on the interseismic fault state, potentially further amplifying differences in shear
 354 resistance evolution for different points along the fault (e.g., nucleation points vs. locked
 355 points) that our simulations already highlight.

356 The presence of time-dependent healing as well as persistent, potentially unper-
 357 ceivable, slow (quasi-static) motion and its acceleration under variable levels of shear stress
 358 illustrate how the concepts of failure, and hence strength, are not easily defined for fric-
 359 tional sliding. For realistic frictional interfaces, the precise value of a static friction co-
 360 efficient is ill-defined, since no interface loaded in shear is perfectly static; rather creep
 361 processes occur at slow, unperceivable slip rates at any level of shear loading (Dieterich
 362 & Kilgore, 1994; Bhattacharya et al., 2017) and/or over parts of the contacting inter-
 363 faces (Rubinstein et al., 2004, 2006; Ben-David et al., 2010). Hence the transition from
 364 locked interfaces to detectable slip is always a gradual process (although it may be oc-
 365 ccurring faster than the time scales of interest/observation in many applications). This
 366 reality is reflected in lab-derived fault constitutive relations such as rate-and-state fric-
 367 tion. Since failure typically refers to the presence of irreversible or inelastic deformation,
 368 frictional interfaces may be considered failing under any style or rate of motion, be it dur-
 369 ing slow steady sliding, transient slow slip, or dynamic rupture. Therefore, any mean-
 370 ingful notion of strength first requires definition of the failure of interest, e.g., reaching
 371 seismic slip rates of the order of 1 m/s. Without such explicit definition, failure is then
 372 implicitly defined as transition from locked to slipping and corresponds to sliding with
 373 a detectable velocity; for laboratory experiments or observational studies, this would im-
 374 ply that whether the interface is locked or slipping depends on the instrumental preci-
 375 sion for detectable motion.

376 In this study, we would like to compare the shear stress values required for aseis-
 377 mic slip nucleation and for dynamic rupture propagation. During spontaneous aseismic
 378 slip nucleation, the slip rates evolve from very low to seismic, passing in the process through
 379 the slip rate equal to the tectonic loading rate V_{pl} . In the standard rate-and-state fric-
 380 tion, at each fixed sliding rate V , the friction coefficient eventually evolves to a steady-
 381 state value $f_{ss}(V)$ (equation S2; for very small slip rates, the regularized formulation of
 382 equation S5 needs to be considered). Under slow loading, aseismic earthquake nucleation
 383 on a finite fault is typically a gradual process, with many points within the nucleation

384 zone being close to the steady state (Figure 4; Rubin & Ampuero, 2005; Kaneko & La-
 385 pusta, 2008). While the steady-state values of friction depend on the sliding rate, the
 386 dependence is relatively minor at the low, quasi-static slip rates between the plate rate
 387 of approximately 10^{-9} m/s and sub-seismic slip rates of $< 10^{-3}$ m/s (Figure 1) which
 388 are relevant for fault creep and earthquake nucleation, and for which the standard rate-
 389 and-state formulation is (approximately) valid. The product of this collection of steady-
 390 state quasi-static friction coefficients and the interseismic drained effective stress gives
 391 the shear resistance of faults at sustained slow sliding rates, which we call the *steady-*
 392 *state quasi-static fault shear resistance* (referred to in short as local SSQS shear resis-
 393 tance). As the representative value of such local SSQS shear resistance, we choose the
 394 shear resistance of the fault steadily creeping at the prescribed long-term tectonic plate
 395 rate V_{pl} (which the fault would have long-term if it were slipping stably), with the in-
 396 terseismic drained value of the pore pressure p_{int} :

$$\tau_{ss}^{V_{\text{pl}}}(z, t) = (\sigma - p_{\text{int}}) f_{ss}(V_{\text{pl}}) \quad (4)$$

397 In our models, $\tau_{ss}^{V_{\text{pl}}} / (\sigma - p_{\text{int}}) = 0.63$ within the VW region. Note that choosing V_* in-
 398 stead of V_{pl} would result in a similar value of $\tau_{ss}^{V_{\text{pl}}} / (\sigma - p_{\text{int}}) = f_* = 0.6$.

399 In the following section, we compare this representative value of local SSQS shear
 400 resistance to the spatial distribution of shear stress prior to dynamic ruptures in our sim-
 401 ulations. Note that the local SSQS shear resistance is similar to what is typically viewed
 402 as "frictional fault strength" in the sense of Byerlee (1978), i.e., this is the resistance that
 403 needs to be met for noticeable quasi-static slip with the loading rate or another refer-
 404 ence rate.

405 **4 Larger ruptures associated with lower shear prestress over the rup-**
 406 **ture scale but higher prestress over smaller scales near nucleation**

407 The interseismic periods in between individual earthquake ruptures in our simu-
 408 lations vary from months to decades, depending on the size of the rupture and the stress
 409 state resulting from the history of prior slip along the fault. Our earthquake sequence
 410 simulations produce a wide variety of rupture sizes due to heterogeneous prestress con-
 411 ditions along the fault that spontaneously arise in our models.

412 Let us consider the evolution of slip and shear stress in representative simulated
 413 spontaneous ruptures of increasing sizes within the same simulation (Figure 6). Over se-
 414 quences of rupture events, the shear stress conditions prior to and after individual dy-
 415 namic ruptures become spatially heterogeneous. This stress heterogeneity is due in part
 416 to the history of spatially variable slip and local static stress drop produced in previous
 417 ruptures, as well as stress relaxation and redistribution due to aseismic slip. In addition,
 418 while our simulated fault models are loaded by a constant long-term loading rate of V_{pl} ,
 419 the effective loading conditions along the fault interface vary in space and time due to
 420 differences in slip rate along the fault. Ruptures nucleate preferentially in regions with
 421 the highest shear prestress, which in our models occur near the creeping regions as dis-
 422 cussed in section 3 (Figure 6). The ruptures then propagate into the less stressed areas
 423 of the fault. Put another way, the average prestress over the nucleation region is higher
 424 than the average prestress over the entire ruptured region (Figure 7A vs. B), as we quan-
 425 tify in the following.

426 We compute the average shear prestress right before a dynamic rupture event over
 427 the entire future rupture area (which we do as post-processing of data in our simulation).
 428 We also compute the average shear prestress over the slow-slip nucleation zone, which
 429 we call the *nucleation stress*. We compare these average shear stress measures with the
 430 *local steady-state quasi-static (SSQS) fault shear resistance* $\tau_{ss}^{V_{pl}}$, which is related to the
 431 local fault constitutive properties during slow slip and given by equation 4.

432 Averaging of spatially variable stress fields can be done in several different ways
 433 (Noda & Lapusta, 2012; Noda et al., 2013). The simplest definition of the average shear
 434 prestress over the rupture region Ω is the spatially averaged prestress τ_{ini}^A , acting in the
 435 overall slip direction at the beginning of the rupture t_{ini} , given by:

$$\tau_{\text{ini}}^A = \frac{\int_{\Omega} \tau(z, t_{\text{ini}}) dz}{\int_{\Omega} dz}. \quad (5)$$

436 We can similarly define the spatially averaged nucleation stress τ_{nuc1}^A within the nu-
 437 cleation region. We define the nucleation region to be the fault segment between the ex-
 438 panding stress fronts at the initiation of dynamic rupture; the size of the nucleation re-
 439 gions in our simulations is comparable to the theoretical nucleation size estimate h_{RA}^*
 440 of Rubin and Ampuero (2005) (equation S6, Figure S1).

441 Not surprisingly and consistent with prior studies, we find that the spatially av-
 442 eraged nucleation stress τ_{nuc1}^A for our simulated ruptures is comparable to the local SSQS
 443 shear resistance τ_{ss}^{Vpl} (Figure 7A). As a consequence, it does not significantly depend on
 444 the ultimate rupture size or slip. Since the nucleation stress here is computed at the be-
 445 ginning of dynamic rupture, it is then the shear stress within the nucleation zone at the
 446 end of the nucleation, when parts of the zone slip with near-dynamic slip rates approach-
 447 ing 10^{-2} m/s. That is why the nucleation stress is systematically slightly lower than the
 448 local SSQS shear resistance defined as the steady-state shear resistance to slip with the
 449 (lower) plate rate. The difference between the nucleation stress and local SSQS shear
 450 resistance could be more substantial if dynamic weakening were efficient enough to af-
 451 fect some portion of the earthquake nucleation region (Segall & Rice, 2006).

452 In contrast, the spatially averaged prestress over the entire ruptured area τ_{ini}^A tends
 453 to decrease with the rupture size and increasingly deviate from the local SSQS shear re-
 454 sistance and nucleation stress for increasingly efficient dynamic weakening (Figures 6 &
 455 7B). Such behavior is also true for another average prestress measure, the energy-based

456 average prestress $\bar{\tau}_{\text{ini}}^E$ (Noda & Lapusta, 2012), which is the average shear prestress weighted
 457 by the final slip of the rupture, and hence represents the average prestress associated with
 458 the potency of the impending rupture:

$$\bar{\tau}_{\text{ini}}^E = \frac{\int_{\Omega} \tau(z, t_{\text{ini}}) \delta_{\text{fin}}(z) dz}{\int_{\Omega} \delta_{\text{fin}}(z) dz} \quad (6)$$

459 where $\delta_{\text{fin}}(z) = \delta(z, t_{\text{fin}}) - \delta(z, t_{\text{ini}})$ is the final local slip accrued in the rupture. We
 460 denote $\bar{\tau}^E$ with a bar as it not only represents an average over space but also requires
 461 knowledge of the final slip of the rupture. $\bar{\tau}_{\text{ini}}^E$ differs from the spatially-averaged pre-
 462 stress τ_{ini}^A over the rupture area when the resulting slip distribution is not uniform. We
 463 find that $\bar{\tau}_{\text{ini}}^E$ and τ_{ini}^A for our simulated ruptures are comparable and vary similarly with
 464 the rupture size and efficiency of dynamic weakening, with the values of $\bar{\tau}_{\text{ini}}^E$ being slightly
 465 larger (Figure S2).

466 The finding that larger ruptures are associated with smaller average shear prestress
 467 over the ruptured area may appear counterintuitive. Why do smaller ruptures not be-
 468 come larger if they are more favorably prestressed? To understand this behavior, let us
 469 consider the prestress averaged over several fixed scales around the nucleation region for
 470 ruptures of different sizes. We locate the VW-VS boundary next to which each of our
 471 simulated ruptures nucleate and average the prestress along the VW region over fixed
 472 distances (1, 2, 4, 8, 12 and 16 km) from the corresponding VW-VS boundary (Figure
 473 8; shown for fault model TP4 from Table 2). While the spatially-averaged prestress over
 474 the entire rupture length decreases with increasing rupture size, we see that the prestress
 475 spatially-averaged over smaller fixed scales is generally higher for larger ruptures than
 476 for smaller ruptures (Figure 8 warmer vs cooler colored triangles). For smaller ruptures,
 477 the average shear stress over scales just larger than their total rupture length is lower
 478 than the average prestress of larger ruptures with comparable length to the fixed aver-
 479 aging scales (Figure 8, triangles below the circles). This confirms that the smaller rup-
 480 tures arrest because the prestress conditions ahead of the rupture are too low to sustain

481 further rupture propagation. For larger ruptures, the average prestress levels at scales
482 smaller than their total rupture length are generally higher or comparable to the aver-
483 age prestress over smaller ruptures with the length comparable to the fixed averaging
484 scales (Figure 8, triangles above the circles). This finding suggests that larger ruptures
485 have higher, more favorable average prestress conditions at smaller scales compared to
486 smaller ruptures, which facilitates continued rupture propagation. Hence we find that
487 the shear prestress prior to our simulated ruptures of varying sizes self-organizes into a
488 spatial distribution of scale-dependent average shear stress that governs the rupture oc-
489 currence.

490 **5 Role of dynamic stress transfers and motion-dependent local shear** 491 **resistance**

492 Such scale- and motion-dependent average fault shear prestress before ruptures re-
493 sults from two related and interacting factors. First, as dynamic rupture propagates, some
494 of the released energy is carried by waves along the fault, creating a substantial stress
495 concentration near the rupture tip that is a well-known feature of dynamic rupture (e.g.,
496 Freund, 1990). The stress concentration enables rupture propagation over regions where
497 the prestress is lower than the local SSQS shear resistance, drawing the local shear stress
498 up to the peak stress before the subsequent stress drop due to local weakening (black
499 lines in Figure 6). The dynamic stress concentration increases with the rupture dimen-
500 sion and/or slip and thus allows larger ruptures to continue propagating over regions with
501 lower, and hence less favorable, prestress conditions (Figure 6). This is illustrated in this
502 work for largely crack-like ruptures that occur in the presented models with mild to mod-
503 erate enhanced dynamic weakening (Lambert et al., in press), but similar conclusions
504 would be reached for pulse-like ruptures provided that they satisfy the observational con-
505 straint of magnitude-independent stress drops, which implies that ruptures with larger
506 magnitudes would have larger average slip and hence larger stress concentrations. Note
507 that a pulse-like rupture with the same or similar spatial distribution of the slip rate (and

508 hence the same local slip) propagating along the fault would result in a similar stress con-
509 centration at the rupture tip regardless of the rupture length; however, in that scenario,
510 pulses with larger rupture propagation lengths would have systematically lower static
511 stress drops, as the stress drops would be proportional to the (uniform) pulse slip divided
512 by ever increasing propagation lengths.

513 Second, the evolving local shear resistance substantially depends on both the prior
514 history of slip events on the fault through fault prestress and on the motion during the
515 current rupture event through dynamic stress transfers that add substantial time-dependent
516 loading. This pronounced dependence is due to strong coupling between the evolving mo-
517 tion, the resulting shear heating, and the evolving shear resistance. As a result, the evo-
518 lution of local slip rate and local shear resistance (1) significantly differs at different fault
519 locations of each rupture (despite uniform constitutive properties) and (2) significantly
520 differs at the same fault location for different ruptures (Figures 2D-I and 6D-E).

521 These two factors create a substantial positive feedback, in which larger ruptures
522 with more slip generate larger stress concentrations, leading to faster and larger slip, which
523 dynamically causes more fault weakening, which in turn promotes more/faster slip, more
524 energy release, larger stress concentrations, and increasing rupture sizes.

525 The result that larger ruptures are associated with lower average prestress indicates
526 the need for increasingly less favorable stress conditions to arrest growing ruptures. For
527 a given rupture size, if the prestress ahead of the rupture is favorable, then the rupture
528 would continue to grow until it experiences sufficiently unfavorable prestress conditions,
529 thus lowering the overall average prestress. Alternatively, the rupture may be forcibly
530 arrested by other means such as strong geometric or rheological barriers. For example,
531 ruptures propagating over higher prestress conditions within the VW region can be ar-
532 rested by fault regions with VS properties; in those cases, the overall average prestress
533 conditions would depend on the properties of the VS regions (Perry et al., 2020). De-

534 tailed study of the implications of fault geometry and heterogeneity for rupture arrest
535 and the average stress conditions prior to rupture is an important topic for future work.

536 **6 Comparison of finite-fault modeling to single-degree-of-freedom rep-** 537 **resentations**

538 As captured in field observations of natural earthquakes and reflected in our sim-
539 ulations, sufficiently large earthquake ruptures nucleate on a subsection of the fault and
540 then propagate through other sections of the fault. Capturing such space-dependent be-
541 havior is typically called "finite-fault" modeling, in contrast to the point source that con-
542 siders a spatially average representation of an event, as if it occurs at one "point". A typ-
543 ical numerical model of a point source is the single-degree-of-freedom system (SDOF)
544 of a slider with friction pulled by a spring (e.g. Dieterich, 1979; Ruina, 1983; Rice & Ru-
545 ina, 1983). Small-scale laboratory experiments often measure properties averaged over
546 a sample and are typically modeled as a SDOF spring-slider systems.

547 The significant role of spatially varying prestress conditions and dynamic stress trans-
548 fers during rupture propagation in determining the rupture behavior implies that cap-
549 turing the finite-fault nature of the process is essential for determining the stress evo-
550 lution characteristic of dynamic rupture. For example, several laboratory studies applied
551 variable slip rates histories inferred from natural earthquakes to rock samples, measured
552 the resulting shear resistance, and then related laboratory stress measurements to seis-
553 mological source properties such as breakdown energy and stress drops (e.g. Sone & Shi-
554 mamoto, 2009; Fukuyama & Mizoguchi, 2010; Nielsen et al., 2016). Such experiments
555 have provided invaluable data about the local shear resistance of faults, specifically en-
556 hanced dynamic weakening, that have informed theoretical and numerical modeling of
557 finite faults (e.g. Zheng & Rice, 1998; Rice, 2006; Noda et al., 2009; Noda & Lapusta,
558 2010; Dunham et al., 2011; Gabriel et al., 2012; Perry et al., 2020; Lambert et al., in press),
559 including the current study. However, the interpretation of such experiments needs to

560 take into account their SDOF nature. For example, to improve alignment etc, the ex-
561 periments often impose pre-sliding at slow slip rates (of the order of micron/s) prior to
562 imitating seismic motion. That procedure results in the shear prestress before seismic
563 slip comparable to the local SSQS shear resistance (equation 4) and near steady-state
564 values of the state variable, as appropriate for a location within a nucleation zone. In
565 contrast, our simulations show that most points on a fault through which the rupture
566 propagates have much lower shear prestress and much larger values of the state variable
567 corresponding to well-healed fault (Figures 6 and 9B). Furthermore, the experiments of-
568 ten apply smoothed slip-rate histories obtained from finite-fault inversions, while the
569 stress concentration at the tip of dynamic rupture makes the slip rate variation much
570 more dramatic.

571 To illustrate the differences for the shear resistance evolution obtained with such
572 experimental procedures versus the one from our simulated finite-fault models, let us com-
573 pare the local fault behavior during one of our dynamic ruptures with a SDOF calcu-
574 lation. In the SDOF calculation, we use the same fault properties (equations 3, S4 and
575 S7-8) and same parameter values as in the finite-fault VW regions but apply quasi-static
576 presliding and modified, smoothed slip rates motivated by the laboratory procedures
577 of Fukuyama and Mizoguchi (2010) (further details in Supplementary Materials). We
578 conduct the comparison for two fault locations, one in the nucleation region and one within
579 dynamic rupture propagation region (Figure 9). These SDOF calculations are success-
580 ful at reproducing the presence of the enhanced dynamic weakening with slip as occurs
581 during dynamic ruptures and generally capture the more moderate slip evolution and
582 behavior of points within the nucleation region of our simulated dynamic ruptures. At
583 the same time, the overall shear stress evolution during typical propagation of the dy-
584 namic rupture substantially differs from that of the SDOF calculation, with notable fea-
585 tures including the low initial stress (which depends on prior slip history) relative to the
586 SSQS shear resistance, the much more dramatic increase in shear stress associated with
587 the dynamic rupture front (which arises due to the more healed fault coupled with the

588 dynamic stress concentration), and the shear stress evolution at the end of slip (which
589 depends on the final slip distribution over the entire finite fault) (Figure 9).

590 **7 Implications for earthquake statistics**

591 A notable feature of the scale dependence of average prestress before dynamic rup-
592 ture is that, as an earthquake grows larger, the prestress needed for further propagation
593 decreases (Figure 7B). In addition, the higher the weakening rate, the easier it should
594 be for a rupture to have favorable prestress conditions to continue growing, rather than
595 arresting as a smaller earthquake. Hence one could hypothesize that the more efficient
596 the enhanced dynamic weakening, the smaller the complexity of the resulting earthquake
597 sequences, with increasing representation of larger events at the expense of smaller events.

598 This is exactly what our modeling shows (Figure 10). The fault models with in-
599 creasingly more efficient weakening produce earthquake sequences with increasingly fewer
600 small events and decreasing b-values of the cumulative size distribution (Figure 10). Fault
601 models with even more efficient dynamic weakening than considered in this study, such
602 as those that produce sharp self-healing pulses, result in relatively simple earthquake se-
603 quences consisting of only large events (Lambert et al., in press). The fault models gov-
604 erned by relatively mild to more moderate weakening as considered in this work develop
605 a wider range of earthquake sizes, due to a feedback loop of more likely rupture arrest
606 due to milder weakening creating stress heterogeneity that in turn makes rupture arrest
607 more likely. This result is consistent with those of previous quasi-dynamic earthquake
608 sequence simulations demonstrating complex earthquake sequences with b-values around
609 0.75 on faults with standard rate-and-state friction only and milder quasi-dynamic stress
610 transfer (Cattania, 2019). Our study shows that the b-values decrease to 0.5 for fully
611 dynamic simulations without enhanced dynamic weakening, and further decrease to 0.25
612 or so for the most efficient weakening considered in this study.

613 While the frequency-magnitude distribution of seismicity over relatively large re-
614 gions, such as Northern or Southern California, is generally well-described by Gutenberg-
615 Richter scaling with typical b-values near unity (E. Field et al., 2013), whether such scal-
616 ing applies to individual fault segments and/or their immediate surroundings is a topic
617 of active research (Wesnousky, 1994; Ishibe & Shimazaki, 2012; Kagan et al., 2012; Page
618 & Felzer, 2015; Page & van der Elst, 2018; E. H. Field et al., 2017). Estimates of b-values
619 associated with individual fault segments can exhibit considerable variability (e.g. be-
620 tween 0.5 and 1.5 along faults in California; Tormann et al., 2014), and are sensitive to
621 a number of factors, including the magnitude of completeness of the relevant earthquake
622 catalog and the choice of observation region and time window (Tormann et al., 2014; Page
623 & Felzer, 2015; Ishibe & Shimazaki, 2012; Page & van der Elst, 2018). A number of stud-
624 ies suggest that the rate of large earthquakes on major faults, such as the San Andreas
625 Fault, is elevated above what would be expected given typical Gutenberg-Richter scal-
626 ing from smaller magnitude events (Schwartz & Coppersmith, 1984; E. H. Field et al.,
627 2017). In particular, some mature fault segments that have historically hosted large earth-
628 quakes, such as the Cholame and Carrizo segments of the San Andreas Fault, exhibit sub-
629 stantial deviations from typical Gutenberg-Richter scaling, being nearly absent of small
630 earthquakes (Sieh, 1978; Wesnousky, 1994; Bouchon & Karabulut, 2008; Hauksson et al.,
631 2012; Jiang & Lapusta, 2016; Michailos et al., 2019). Our findings suggest that the paucity
632 of microseismicity on such mature fault segments may indicate that they undergo sub-
633 stantial dynamic weakening during earthquakes ruptures.

634 **8 Discussion**

635 Our simulations demonstrate that the average shear prestress required for rupture
636 propagation can be considerably lower than the average shear stress required for the rup-
637 ture nucleation. This is because the quasi-static nucleation process is governed by rel-
638 atively small stress changes and hence requires favorable prestress conditions - close to
639 the local steady-state quasi-static shear resistance - to proceed. In contrast, during dy-

640 namic rupture, the rupture front is driven by larger wave-mediated dynamic stress con-
 641 centrations, which are more substantial for larger ruptures and facilitate rupture prop-
 642 agation over less favorably stressed regions, resulting in the spatially-averaged prestress
 643 over the ruptured area being much lower than the average local SSQS shear resistance.
 644 More efficient weakening facilitates larger dynamic stress changes at the rupture front,
 645 allowing propagation over even less favorable prestress conditions. Our results highlight
 646 the significance of heterogeneity in prestress, or shear resistance, for the nucleation and
 647 ultimate arrest of finite ruptures, even in fault models that have otherwise uniform ma-
 648 terial and confining properties.

649 The decrease in averaged prestress with rupture length can be interpreted as a de-
 650 crease in the average quasi-static friction coefficient $\tau_{\text{ini}}^A/(\sigma - p_{\text{int}})$ with rupture size (Fig-
 651 ure 7). The average quasi-static friction coefficients for ruptures on the scale of the nu-
 652 cleation size are consistent with the prescribed quasi-static reference friction coefficient
 653 near typical Byerlee values. However, as we average the prestress over larger rupture lengths,
 654 the average quasi-static friction coefficient can considerably decrease depending on the
 655 efficiency in weakening.

656 The presence of enhanced dynamic weakening draws the average shear stress along
 657 larger regions of the fault below the local SSQS consistent with earthquake nucleation,
 658 resulting in lower average shear stress conditions in terms of both the average prestress
 659 for larger ruptures and the average dynamic resistance associated with shear heating dur-
 660 ing ruptures (Figure 11). The models presented in this study with mild-to-moderate en-
 661 hanced weakening include considerable persistent fluid overpressurization to maintain
 662 low-heat, low-stress conditions with average dynamic shear resistance during seismic slip
 663 rates below 10 MPa; however the degree of fluid overpressure required to maintain low-
 664 heat conditions is less than that with comparable rate-and-state properties but no en-
 665 hanced weakening. The presence of some enhanced dynamic weakening is also needed
 666 for persistently weak fault models due to chronic fluid overpressure in order to ensure

667 that static stress drops are not too small, as they would otherwise be with low effective
668 stress and small changes in the friction coefficient due to standard rate-and-state laws
669 (Figures 11 and S3; Lambert et al., in press). Fault models with more efficient dynamic
670 weakening have been shown to be able to reproduce low-stress operation and reasonable
671 static stress drops with quasi-static friction coefficients around Byerlee values and higher
672 effective normal stress (e.g. ≥ 100 MPa; Noda et al., 2009; Dunham et al., 2011; Lam-
673 bert et al., in press). Earthquake sequence simulations of such fault models typically con-
674 sist of only large ruptures (Lambert et al., in press), consistent with the notion that large
675 fault areas governed by efficient weakening maintain substantially lower average shear
676 stresses than that required for nucleation. These findings further strengthen the conclu-
677 sion of prior studies that enhanced dynamic weakening can help explain the discrepancy
678 between laboratory values of (quasi-static) friction coefficients around 0.6 and geophys-
679 ical inferences of low effective coefficients of friction (< 0.2), along with mild average static
680 stress drops of 1 to 10 MPa, over fault areas that host large earthquakes (e.g Marone,
681 1998; Suppe, 2007; Allmann & Shearer, 2009; Noda et al., 2009; Dunham et al., 2011;
682 Ikari et al., 2011; Gao & Wang, 2014; Ye et al., 2016b; Perry et al., 2020; Lambert et al.,
683 in press).

684 The scale dependence of average prestress before ruptures can also be interpreted
685 as a scale dependence of *average fault strength*, since the average prestress represents a
686 measure of how much shear stress that fault region can hold before failing in a rupture.
687 Given this interpretation, our simulations suggest that faults maintain lower average shear
688 stresses, and hence appear weaker, at larger scales than at smaller scales. This interpre-
689 tation is conceptually consistent with laboratory measurements of scale-dependent yield
690 stress for rocks and a number of engineering materials, which demonstrate decreasing
691 material strength with increasing scale (Jaeger & Cook, 1976; Bandis et al., 1981; Greer
692 et al., 2005; Pharr et al., 2010; Uchic et al., 2004; Yamashita et al., 2015; Thom et al.,
693 2017). Note that our larger simulated ruptures, even with more efficient weakening, still
694 require higher average shear stresses over smaller scales in order to nucleate and grow.

695 Thus the lower average prestress levels that allow continued failure in dynamic ruptures
696 at larger scales only become relevant once the rupture event has already nucleated and
697 sufficiently grown over smaller scales. This consideration suggests that the critical stress
698 conditions for rupture occurrence are governed not by a single stress quantity but by a
699 distribution of scale-dependent stress criteria for rupture nucleation and continued prop-
700 agation. An important implication of our findings is that the critical stress for earthquake
701 occurrence may not be governed by a simple condition such as a certain level of Coulomb
702 stress. Given our findings, in order to reason about the stress conditions critical for a
703 rupture to occur, it is important to consider both the size of the rupture and the weak-
704 ening behavior, and hence the style of motion, that may occur throughout rupture prop-
705 agation.

706 The scale dependence of fault material strength has also been hypothesized to ex-
707 plain the measured scaling of roughness on natural fault surfaces (Brodsky et al., 2016).
708 Dynamic rupture simulations on geometrically irregular faults motivated by such rough-
709 ness measurements have indicated an additional contribution to fault shear resistance
710 arising from roughness drag during rupture propagation (Fang & Dunham, 2013). Fur-
711 ther examination of the scale dependence of average shear resistance across faults includ-
712 ing realistic fault geometry is an important topic for future work.

713 A common assumption is that the shear prestress over the entire ruptured area must
714 be near the local static (or quasi-static) strength, comparable to the SSQS shear resis-
715 tance discussed in this study. We demonstrate that the assumption is not necessarily valid
716 and that faults with enhanced dynamic weakening and history of large earthquake rup-
717 tures would, in fact, be expected to have low average shear stress over large enough scales.
718 At the same time, the state of stress needs to be heterogeneous, with the average stresses
719 over small scales (comparable to earthquake nucleation) being close to the (much higher)
720 local SSQS shear resistance in some places. Thus, while individual measurements of low
721 resolved shear stress onto a fault may suggest that those locations appear to not be crit-

722 ically stressed for quasi-static failure, those regions, and much of the fault, may be suf-
723 ficiently stressed to sustain dynamic rupture propagation and hence large earthquake rup-
724 tures. In addition, our findings suggest that inferences of stress levels on faults may dif-
725 fer if they are obtained over different scales or influenced by different rupture processes.
726 For example, low-stress conditions on mature faults from observations of low heat flow
727 may not only represent average shear stress conditions over large fault segments as a whole
728 but also be dominated by low dynamic resistance during fast slip, whereas averages over
729 smaller scales would be expected to reflect the heterogeneity of the underlying prestress
730 distribution, as perhaps reflected in varying stress rotations inferred over scales of tens
731 of kilometers (Hardebeck & Hauksson, 1999, 2001; Hardebeck, 2015).

732 Our modeling shows that increasingly efficient dynamic weakening leads to differ-
733 ent earthquake statistics, with fewer small events and increasing number of large events.
734 Another factor that can significantly affect the ability of earthquake ruptures to prop-
735 agate is fault heterogeneity. Some dynamic heterogeneity in shear stress spontaneously
736 develops in our simulations, leading to a broad distribution of event sizes for cases with
737 mild to moderate enhanced dynamic weakening. Our findings suggest that the effects
738 of pre-existing types of fault heterogeneity need to be considered with respect to the size
739 of the rupture and weakening behavior on the fault. For example, faults that experience
740 more substantial weakening would require the presence of larger amplitudes of small-wavelength
741 heterogeneity in shear stress or resistance to produce small events. Examining the re-
742 lationship between earthquake sequence complexity and varying levels of fault hetero-
743 geneity and enhanced dynamic weakening is an important topic for future work.

744 **9 Conclusions**

745 Our modeling of faults with rate-and-state friction and enhanced dynamic weak-
746 ening indicates that average shear prestress before dynamic rupture - which can serve
747 as a measure of average fault strength - can be scale-dependent and decrease with the

748 increasing rupture size. Such decrease is more prominent for faults with more efficient
749 dynamic weakening. The finding holds for faults with the standard rate-and-state fric-
750 tion only, without any additional dynamic weakening, although the dependence is rel-
751 atively unremarkable in that case (Figures 7 and S4). However, the scale-dependent de-
752 crease in average prestress is quite pronounced even for fault models with mild to mod-
753 erate enhanced dynamic weakening that satisfy a number of other field inferences, in-
754 cluding nearly magnitude-invariant static stress drops of 1-10 MPa, increasing average
755 breakdown energy with rupture size, radiation ratios between 0.1 and 1.0, and low-heat
756 fault operation (Perry et al., 2020; Lambert et al., in press).

757 Our simulations illustrate that both critical fault stress required for rupture prop-
758 agation and static stress drops are products of complex finite-fault interactions, includ-
759 ing wave-mediated stress concentrations at the rupture front and redistribution of stress
760 post-rupture by dynamic waves. Hence it is important to keep in mind the finite-fault
761 effects - and their consequences in terms of the spatially variable fault prestress, slip rate,
762 and shear stress evolution - when interpreting single-degree-of-freedom representations,
763 such as spring-slider models and small-scale laboratory measurements. This consider-
764 ation highlights the need to continue developing a better physical understanding of fault-
765 ing at various scales through a combination and interaction of small-scale and intermediate-
766 scale lab and field experiments, constitutive relations formulated based on such exper-
767 iments, and finite-fault numerical modeling constrained by inferences from large-scale
768 field observations. Our comparison of local fault behavior in SDOF and dynamic rup-
769 ture simulatons also demonstrate how small-scale experiments can be used in conjunc-
770 tion with finite-fault modeling to improve our understanding of the earthquake source:
771 the finite-fault modeling can suggest the initial conditions and slip-rate histories for the
772 small-scale experiments to impose, and then the shear stress evolution from the small-
773 scale experiments can be compared to the numerically obtained ones, which would al-
774 low to validate and improve the constitutive laws used in finite-fault modeling.

775 We find that increasingly efficient dynamic weakening leads to different earthquake
776 statistics, with fewer small events and increasingly more large events. This finding is con-
777 sistent with the interpretation of average fault prestress before rupture as average fault
778 strength, in that lower fault strength over larger scales leads to an increasing number
779 of larger events. It also adds to the body of work suggesting that enhanced dynamic weak-
780 ening may be responsible for deviations - inferred for large, mature fault segments - of
781 earthquake statistics from the Gutenberg-Richter scaling (Sieh, 1978; Bouchon & Karab-
782 ulut, 2008; Hauksson et al., 2012; Jiang & Lapusta, 2016; Michailos et al., 2019). For ex-
783 ample, fault models with efficient dynamic weakening are consistent with mature faults
784 that have historically hosted large earthquakes but otherwise appear seismically quies-
785 cent, such as the Cholame and Carrizo segments of the San Andreas Fault, which hosted
786 the 1857 Fort Tejon earthquake (Jiang & Lapusta, 2016).

787 Such considerations may be useful for earthquake early warning systems, which cur-
788 rently do not take into account the potential physics-based differences in the event size
789 distribution. Under the assumption of Gutenberg-Richter statistics, the probability that
790 a smaller, Mw 5 or 6 event becomes a much larger earthquake is not great; however, that
791 probability may be substantially larger on mature faults if they are indeed governed by
792 enhanced dynamic weakening.

793 Our results indicate that critical stress conditions for earthquake occurrence can-
794 not be described by a single number but rather present as complex spatial distribution
795 with scale-dependent averages. When considering the critical stress conditions, it is es-
796 sential to take into account both the size of the rupture and the weakening behavior, and
797 hence the style of motion, that may occur throughout rupture propagation. These re-
798 sults warrant further investigation, specifically how the weakening behavior during dy-
799 namic rupture would interact with different degrees of fault heterogeneity as well as im-
800 plications for earthquake early warning.

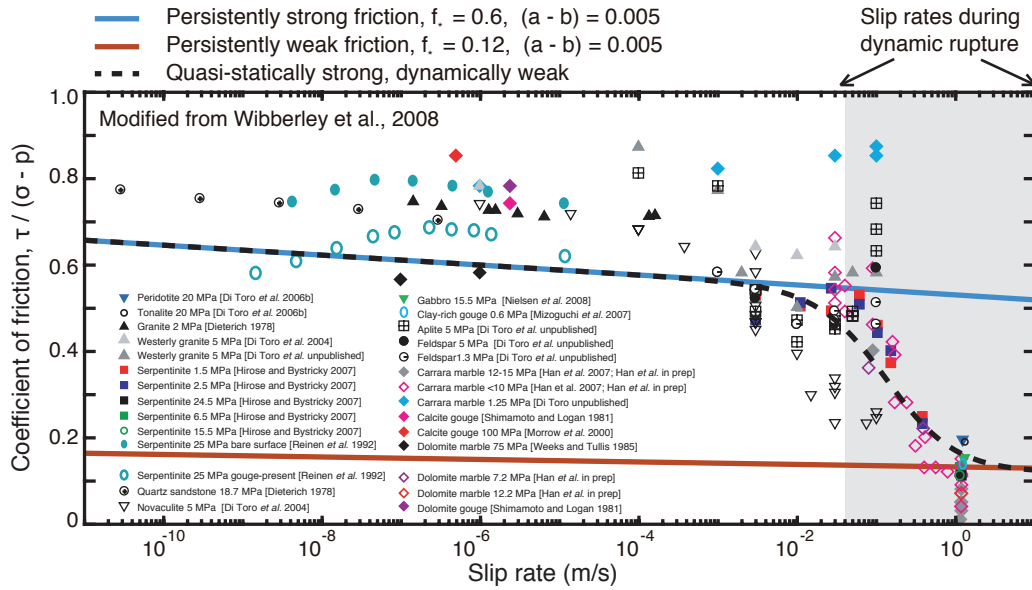


Figure 1. Field observations suggest that the average effective friction on mature faults must be low (< 0.1). One explanation for this inferred low effective friction would be that mature faults are persistently weak, such as from the presence of fault materials with persistently low friction coefficients $\tau/(\sigma - p)$ (red). Faults may also be persistently weak while having actual friction coefficients that are persistently high (> 0.2 , blue), but require substantial chronic fluid overpressure in order to maintain low effective fault friction. A number of laboratory experiments indicate that the coefficient of friction for many materials relevant to seismogenic faults is around 0.6-0.8 at low sliding rates, but drops dramatically to lower values (< 0.2) at higher slip rates relevant to seismic slip, consistent with the notion of quasi-statically strong, but dynamically weak behavior (dashed black line).

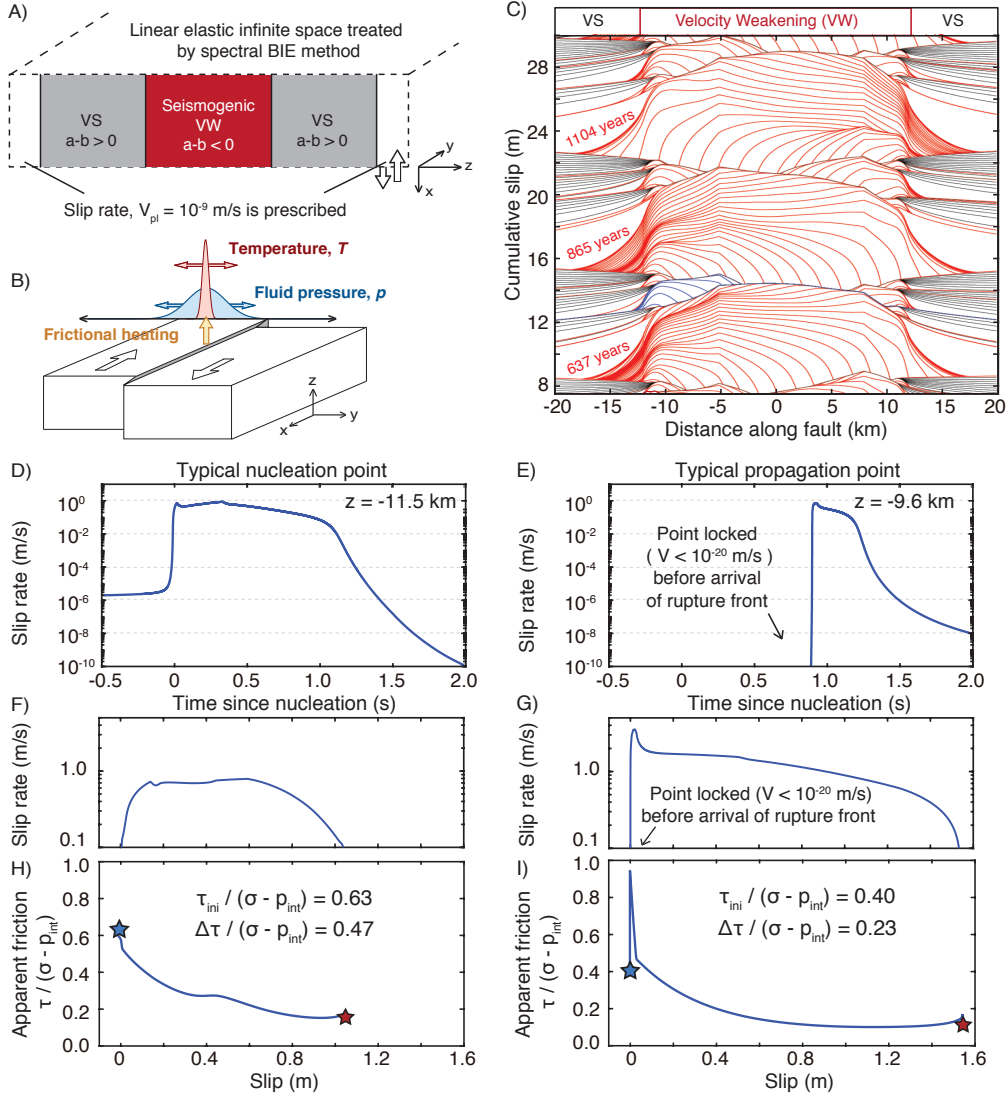


Figure 2. Modeling of sequences of earthquakes and aseismic slip on a rate-and-state fault with (A) a velocity-weakening (VW) seismogenic region surrounded by two velocity-strengthening (VS) sections and (B) enhanced dynamic weakening due to the thermal pressurization of pore fluids. The evolution of temperature and pore fluid pressure due to shear heating and off-fault diffusion is computed throughout our simulations. (C) A short section of the accumulated slip history in fault model TP3 (Table 2). Seismic events are illustrated by red lines plotted every 0.5 s while aseismic slip is shown by black lines plotted every 10 years. (D-G) Evolution of local slip rate with time and slip at points representative of nucleation and typical rupture propagation behavior within a crack-like rupture (colored blue in C). Points throughout rupture propagation (E & G) are initially locked and are driven to rupture by the concentration of dynamic stresses at the rupture front, thus experiencing more rapid acceleration of slip compared to points within the nucleation region (D & F). (H-I) The difference in local slip rate history contributes to a difference in the evolution of shear stress with slip. (H) Evolution of the apparent coefficient of friction $\tau / (\sigma - p_{int})$ with slip in the nucleation region is consistent with the laboratory notion of quasi-statically strong, dynamically weak behavior, with the apparent friction coefficient initially close to the reference value of 0.6 and dropping to a low dynamic resistance below 0.2 with slip. (I) Evolution of the apparent friction coefficient at points throughout rupture propagation is more complicated as the scaled prestress can be much lower than the reference friction before the arrival of the dynamic stress concentration.

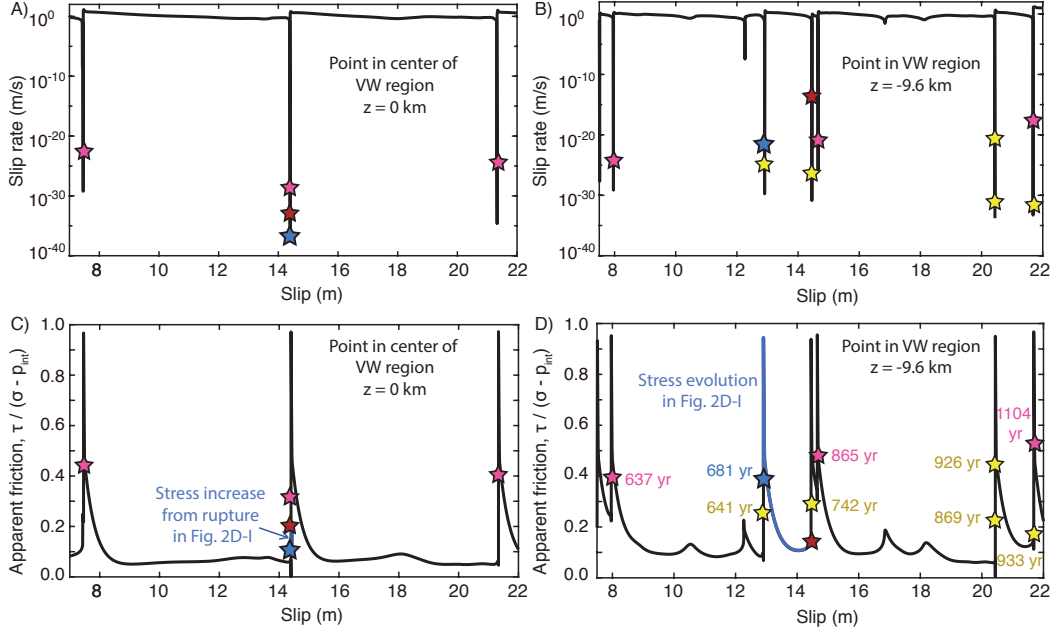


Figure 3. Evolution of the local slip rate and apparent friction coefficient at points within the velocity-weakening (VW) region with accumulating slip in fault model TP3 (Table 2). The stars denote instances in the earthquake sequence in Figure 2C, with pink stars marking the initiation of the three large model-spanning ruptures, the blue and red stars denoting the beginning and end of the moderate-sized rupture illustrated by blue contours, respectively. The yellow stars denote small to moderate-sized ruptures occurring along the VW-VS boundary at $z = -12$ km. (A & C) The point in the center of the VW region ($z = 0$ km) ruptures and experiences substantial slip only in large ruptures. The point exhibits an increase in shear stress over time due to the stress transfer from smaller ruptures that do not penetrate into the center of the VW region (such as the rupture colored blue in Fig. 2C). (B & D) Points closer to the boundary between the VW and VS regions can rupture during both smaller and large ruptures depending on the pre-stress conditions when ruptures arrive, resulting in a more complicated evolution of shear stress with accumulating slip. For both points in the VW region, the shear stress is brought to the peak stress and failure during ruptures by the dynamic stresses at the rupture front.

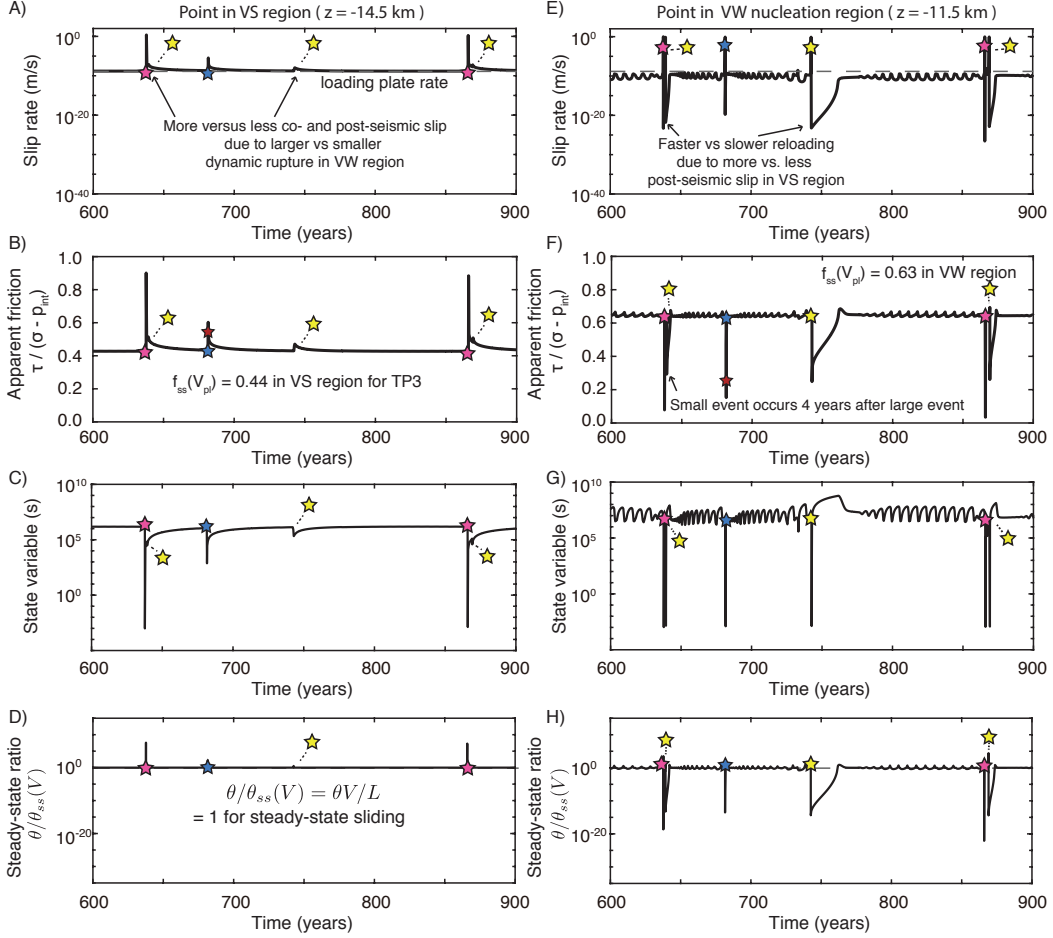


Figure 4. Evolution of local slip rate, apparent friction, and state variable at points near rupture nucleation between two model-spanning ruptures. The stars denote instances in the earthquake sequence in Figure 2C, with pink stars marking the initiation of the first two large model-spanning ruptures, the blue star denoting the beginning of the moderate-sized rupture illustrated by blue contours and the yellow stars denoting smaller ruptures. (A) Points within the VS region typically slip near the loading plate rate but can experience transient accelerated slip during and following ruptures occurring within the VW region. (B-D) The apparent friction coefficient and state variable in the VS region is typically near steady state, except during accelerated slip. (E-F) Slow slip penetrates into the VW region, driving points near the VW-VS boundary close to the loading slip rate, with the apparent friction coefficient being close to the corresponding steady-state value $f_{ss}(V_{pl})$. The slip rate and apparent friction exhibit small oscillations as the points near the VW-VS boundary continue to be loaded by slow slip in the VS region, accelerate, and weaken, thus transmitting stress further into the VW region until a sufficiently large region is loaded to sustain rupture nucleation and acceleration to seismic slip rates. The loading rate of the VW region also depends on the amount of accelerated slip in the VS due to previous ruptures (e.g. A & E around 650 vs. 750 years). (G-H) Following dynamic rupture, the state variable heals close to the steady-state value around the prescribed loading rate $\theta_{ss}(V_{pl})$ but continues to oscillate along with the unsteady slip resulting from the penetration of creep into the VW region, as seen in (E).

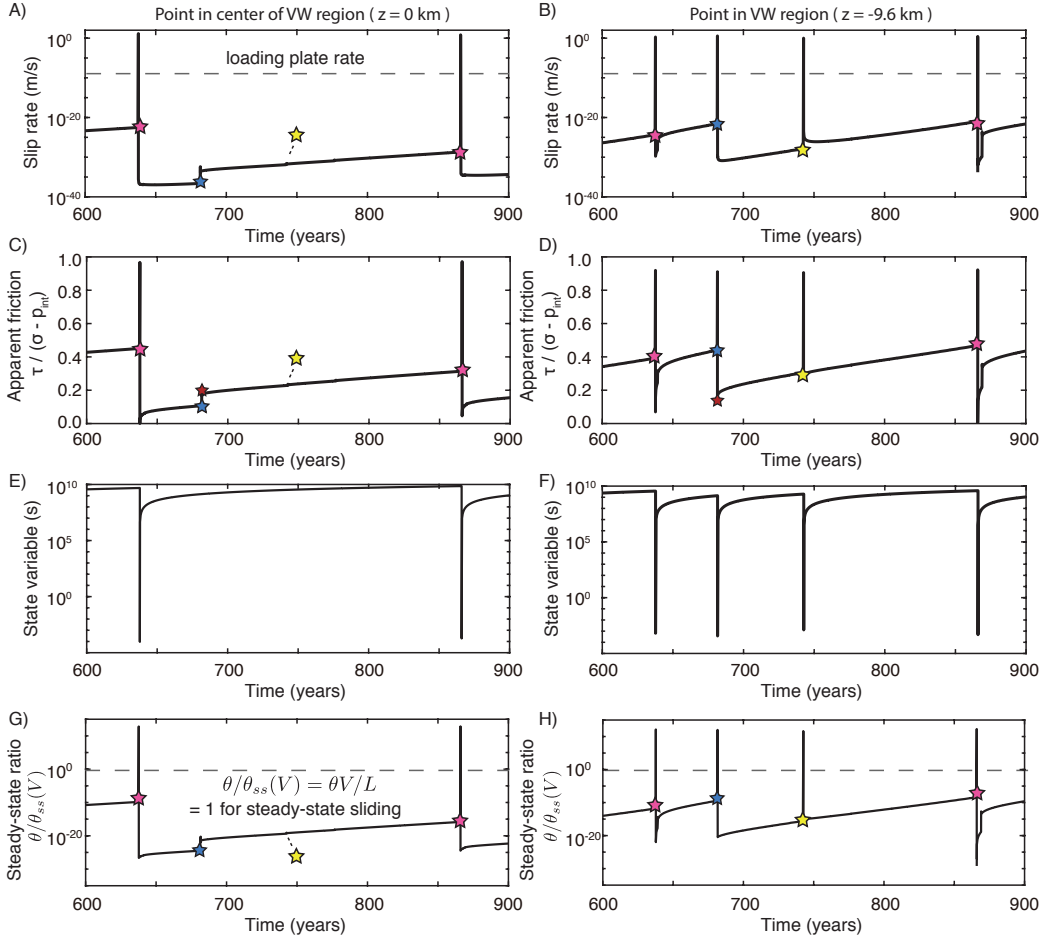


Figure 5. Evolution of local slip rate, apparent friction, and state variable at points within the VW region between two model-spanning ruptures. The stars denote instances in the earthquake sequence in Figure 2C, with pink stars marking the initiation of the first two large model-spanning ruptures, the blue star denoting the beginning of the moderate-sized rupture illustrated by blue contours and the yellow stars denoting smaller ruptures. (A-B) Points within the VW region are typically locked in between earthquake ruptures, sliding at slip rates far below the loading plate rate. (C-D) Loading from the VS regions as well as slip in neighboring ruptures leads to a time-dependent increase in shear stress. However, the points are still near-locked when dynamic rupture arrives from elsewhere, bringing a significant stress concentration and weakening on the timescale of the event which here collapses onto a vertical line. (E-F) The evolution of the state variable shows increase in the interseismic periods which encapsulate the fault healing and decrease to low values during earthquake rupture. (G-H) The ratio of the current value of the state variable θ to the steady-state value $\theta_{ss}(V)$, corresponding to the current local slip rate V , is much smaller than 1 during the interseismic periods, indicating the continued healing of shear resistance prior to rupture. As the slip rate rapidly accelerates during dynamic rupture, the state variable temporarily exceeds the new much lower steady-state values corresponding to the dynamic slip rate $\theta_{ss}(V_{dyn})$, then evolves to this lower steady-state value, and then falls to values below steady-state during the interseismic periods, indicating fault healing.

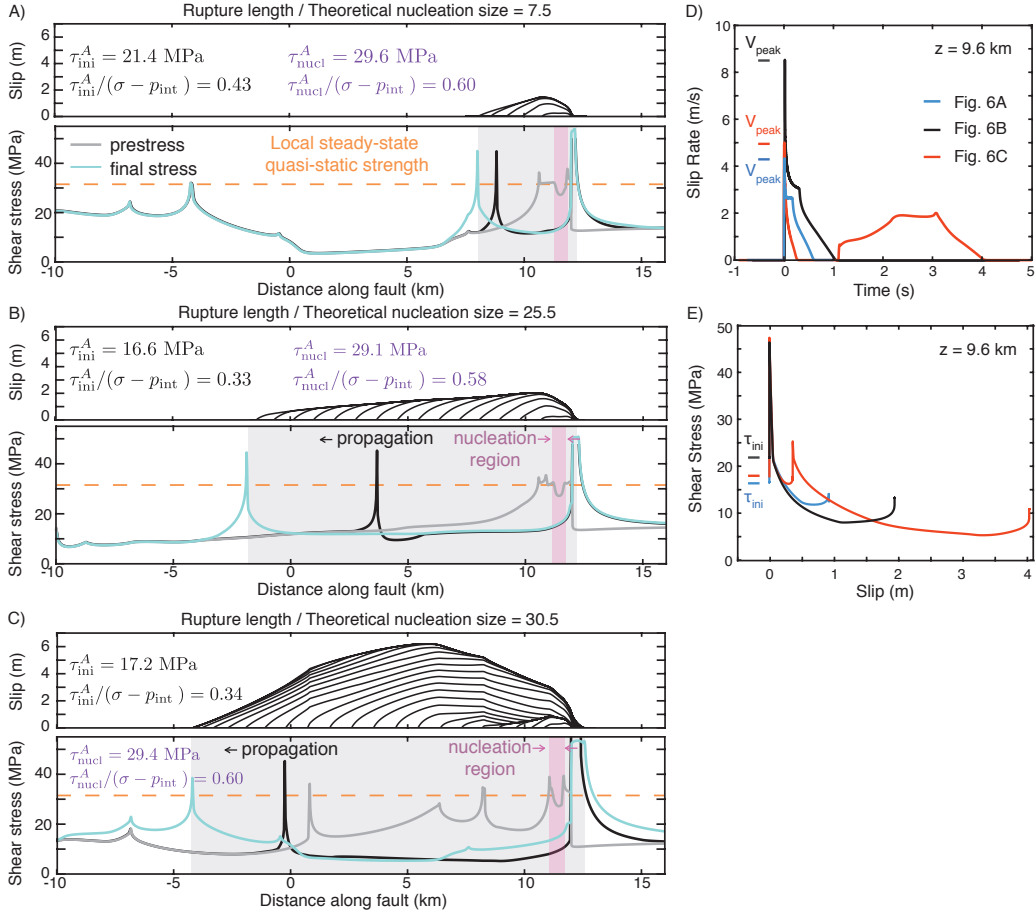


Figure 6. Spatial distribution of slip (top) and prestress and final shear stress (bottom) during three ruptures (A-C) with different rupture lengths in the same fault model (TP4 from Table 2). Slip contours are plotted every 0.25 s. The purple and gray shading illustrates the extent of the nucleation and ruptured regions, respectively, over which the prestress is averaged. While the ruptures nucleate in regions with stress levels near the local steady-state quasi-static shear resistance (dashed orange line), larger ruptures propagate over lower prestressed areas, resulting in lower average prestress and lower average coefficients of friction $\tau_{ini}^A/[\sigma - p_{int}]$. The shear stress distribution for a typical moment during rupture propagation is shown in black, demonstrating the stress concentration at the rupture front that brings the fault stress to values comparable to the SSQS shear resistance. The peak stress is even higher since the fault is initially dynamically stronger due to the rate-and-state direct effect. (D-E) Significant differences in local evolution of slip and stress at the same fault location ($z = 9.6$ km) for different ruptures that depend on the prestress conditions due to previous slip events and the dynamic stress interactions during the individual ruptures.

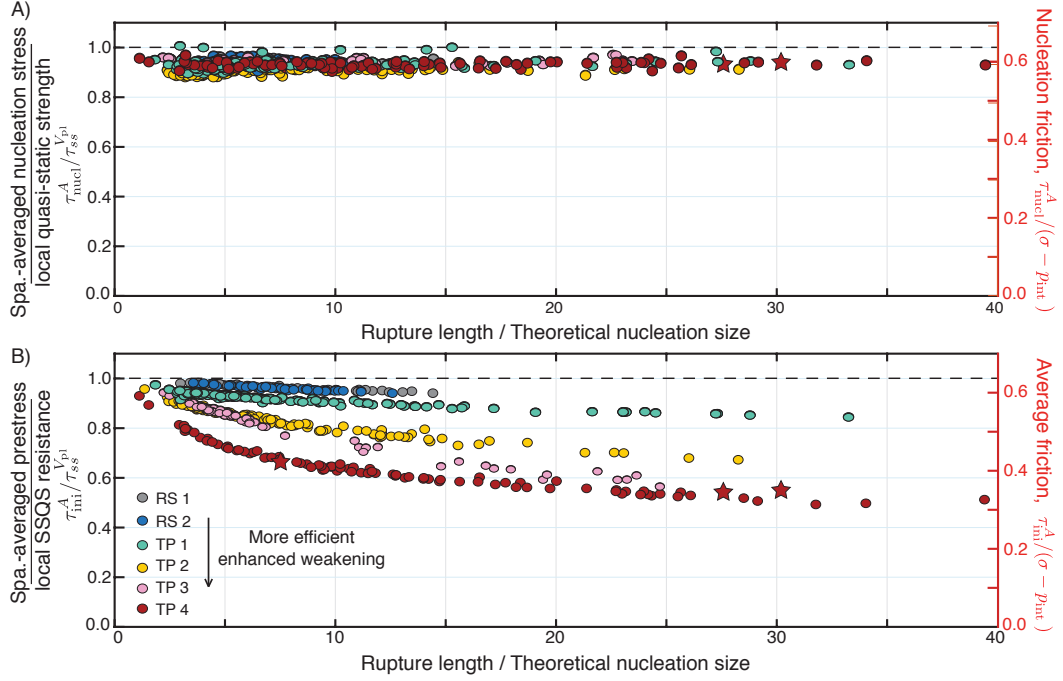


Figure 7. The difference between average shear stress needed for rupture nucleation vs. dynamic propagation. (A) The spatially-averaged nucleation stress τ_{nucl}^A for ruptures is comparable to the average local steady-state quasi-static shear resistance $\tau_{ss}^{V_{p1}}$, regardless of the final rupture size. (B) The spatially-averaged prestress τ_{ini}^A and average friction coefficient $\tau_{\text{ini}}^A / (\sigma - p_{\text{int}})$ decrease with increasing rupture size; the effect is more pronounced with increasing efficiency of weakening. The three ruptures shown in Figure 6 are denoted by red stars.

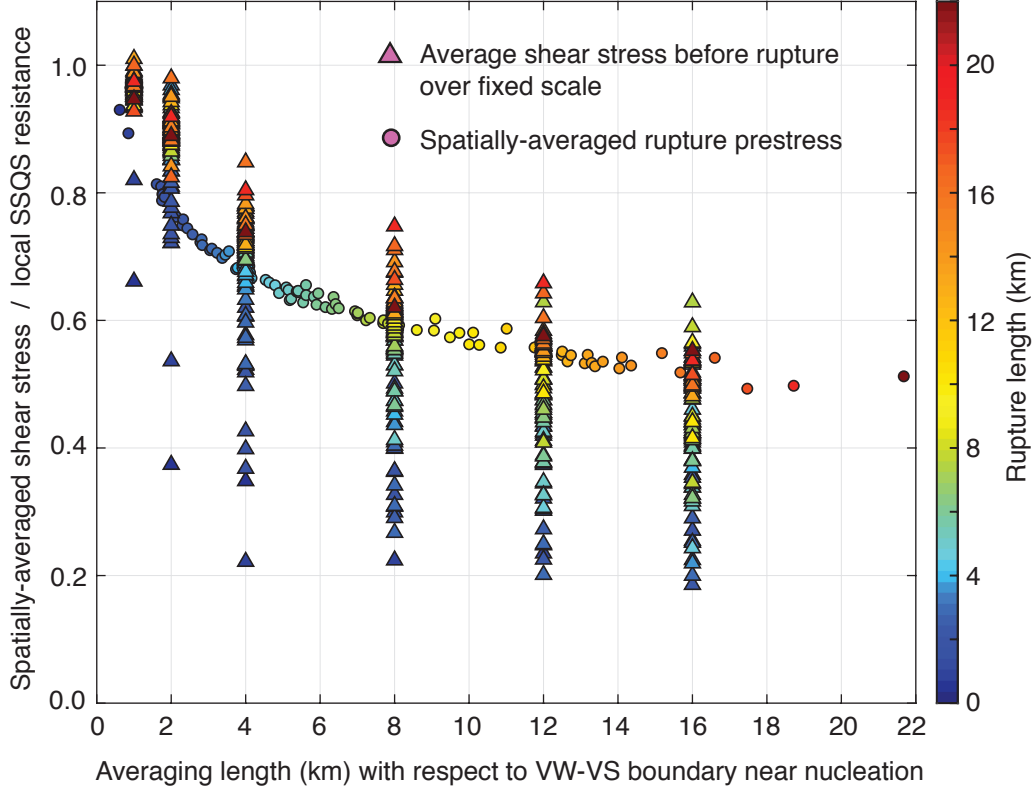


Figure 8. Comparison of the spatially averaged prestress over several fixed scales (1, 2, 4, 8, 12, and 16 km) and the average prestress over ruptures of varying size. As shown in Figure 7, the spatially-averaged prestress over the total rupture area τ_{ini}^A (circles) decreases considerably with rupture size in fault model TP4 from Table 2 with moderate enhanced dynamic weakening. However, larger ruptures have generally higher average shear stresses over smaller fixed scales around the nucleation region compared to smaller ruptures (red vs. blue triangles). The spatially-averaged shear stress over 1 km from the VW-VS boundary near the nucleation region of ruptures (triangles on the far-left) is relatively high (comparable to the local SSQS resistance) for both small and large ruptures, indicating that ruptures nucleate in regions of relatively high prestress compared to the average prestress over the entire rupture area (circles). For smaller ruptures, the average prestress at the fixed scales just larger than their total rupture length is lower than the average prestress of ruptures with comparable length to the fixed scale, suggesting that the prestress levels were too low to sustain further rupture propagation.

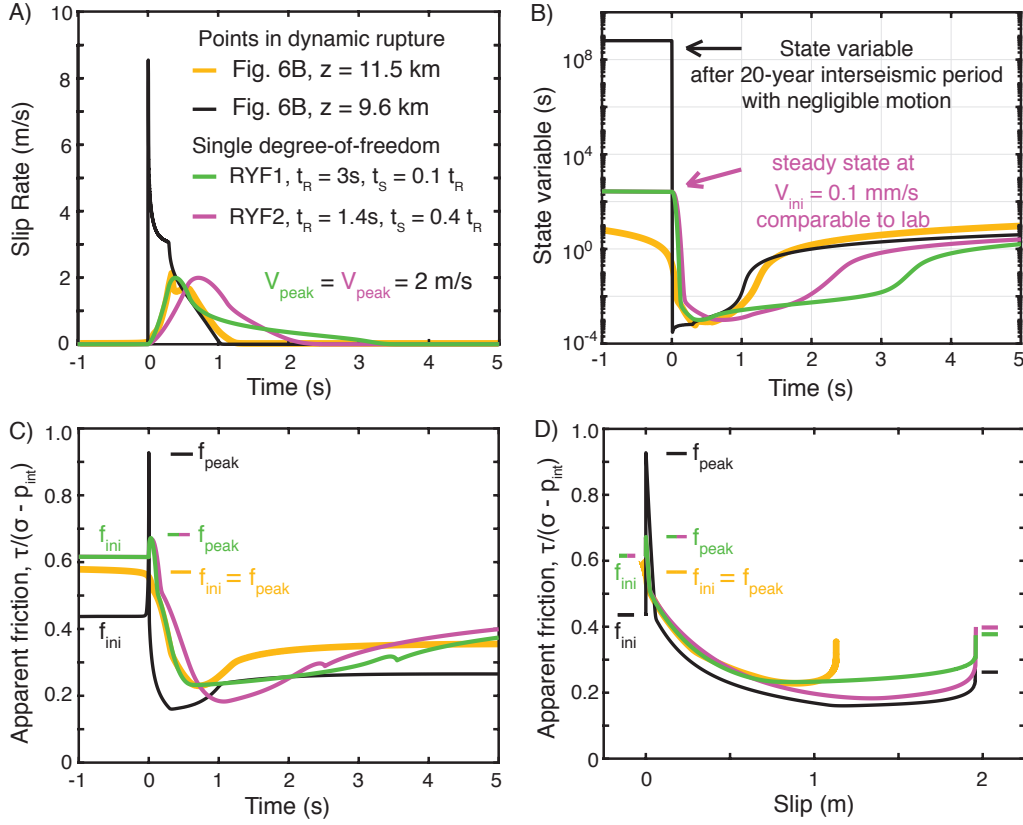


Figure 9. Comparison of the results of our dynamic modeling with what would be obtained in laboratory experiments given the same constitutive properties and typical lab procedures. (A) Comparison of the local slip rate during nucleation ($z = 11.5$ km, yellow) and typical propagation ($z = 9.6$ km, black) of the simulated dynamic rupture of Figure 6B with the slip rate evolution that could be imposed in lab experiments represented by two regularized Yoffe functions (Tinti et al., 2005) with peak slip rate of 2 m/s and comparable slip to the point at $z = 9.6$ km. The imposed regularized Yoffe functions are generally comparable to the evolution of slip within the nucleation region ($z = 11.5$ km), however they do not capture the rapid acceleration of slip associated with the arrival of the rupture front at points of typical propagation, as observed at $z = 9.6$ km. (B) Comparison of the state variable evolution from our simulation and the lab experiment which we simulate using the single-degree of freedom (SDOF) equations. The simulated lab experiment starts with the steady-state conditions for 0.1 mm/s based on the experiments of Fukuyama and Mizoguchi (2010), which results in a much lower initial state value compared to the point $z = 9.6$ km in our simulations which, prior to dynamic rupture, had negligible motion over a 20-year interseismic period. (C-D) Evolution of the local apparent coefficient of friction with time and slip for the point in our simulated finite-fault dynamic rupture and SDOF lab experiments. The dynamic weakening is generally comparable between the points in the finite rupture and the SDOF experiments, however the evolution of shear stress substantially differ with regards to the much lower prestress at $z = 9.6$ km before the finite dynamic rupture and the abrupt increase and then decrease in stress due to the arrival of the dynamic rupture front and the associated rapid weakening.

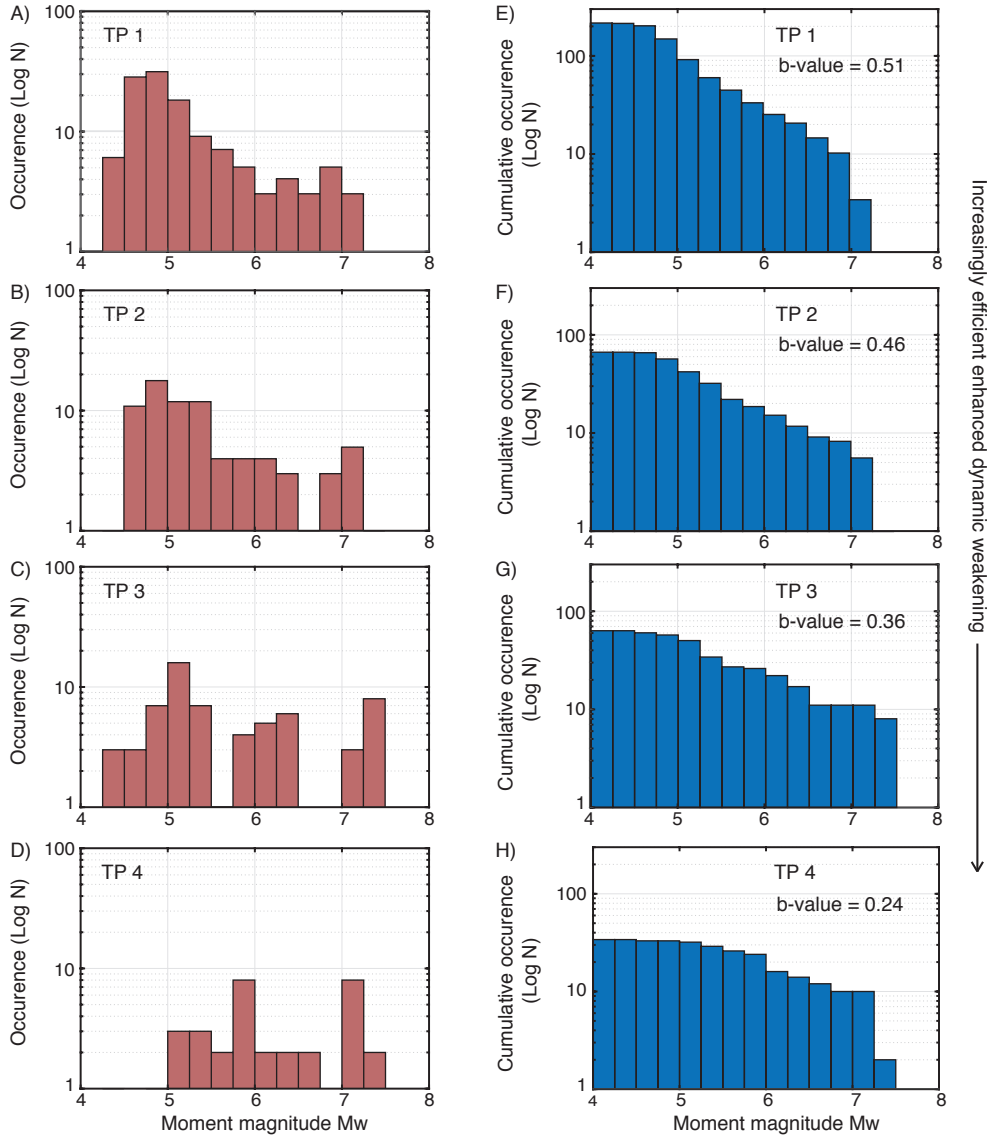


Figure 10. Fault models with more efficient weakening result in less earthquake sequence complexity, producing fewer smaller events (left column) and smaller b-values (right column). (A-D) Frequency-magnitude and (E-H) cumulative frequency-magnitude statistics for simulations with increasing efficiency of enhanced dynamic weakening (TP1-4 from Table 2).

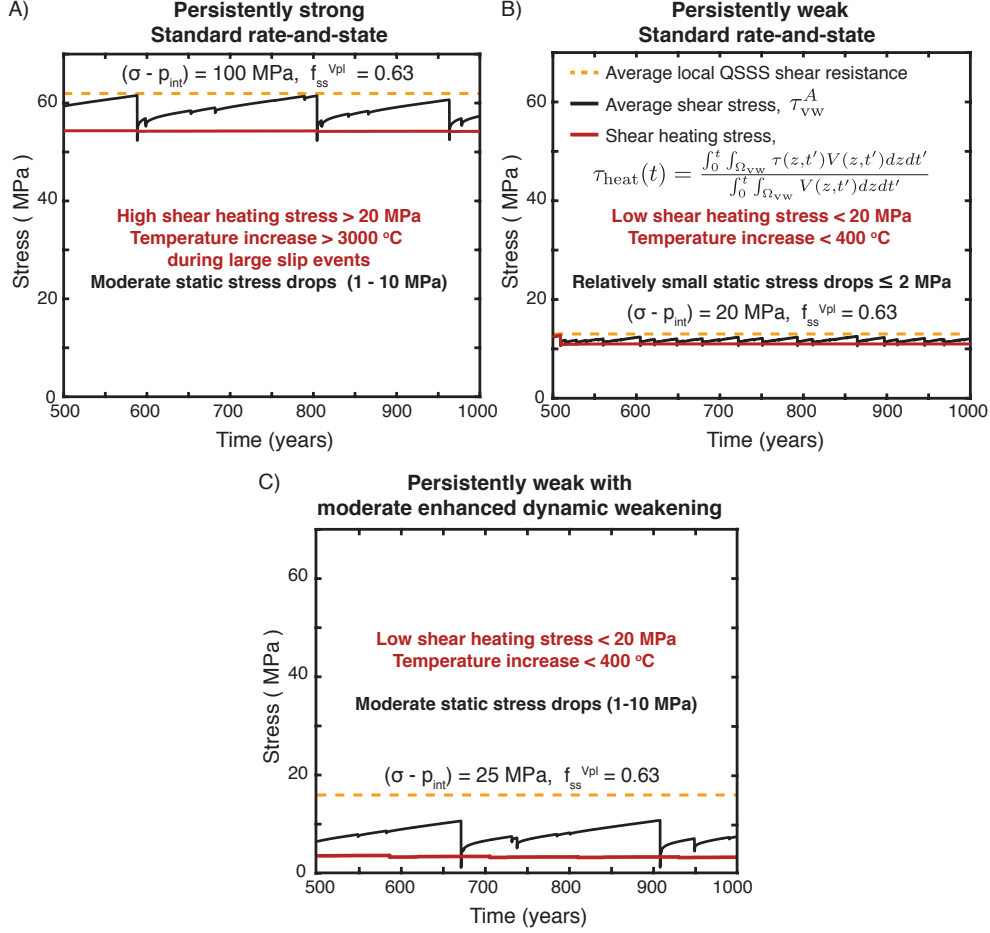


Figure 11. Evolution of the spatially averaged shear stress in the VW region τ_{vw}^A (black line) over earthquake sequences. (A-B) Standard rate-and-state friction results in modest changes in shear resistance from the average local steady-state quasi-static (SSQS) shear resistance (orange line). Ruptures on persistently strong faults produce realistic static stress drops (A); however, the fault temperature would increase by more than 3000 °C during a dynamic event for a shear-zone half-width of 10 mm. (B) Persistently weak fault models due to low effective normal stress but with no enhanced weakening (RS 1 of Table 2) can maintain modest fault temperatures, but produce relatively small static stress drops $\leq 2 \text{ MPa}$. (C) Persistently weak models with mild to moderate enhanced dynamic weakening (TP3 of Table 2) are capable of maintaining modest fault temperatures and producing more moderate average stress drops between 1 - 10 MPa.

Parameter	Symbol	Value
Loading slip rate	V_{pl}	10^{-9} m/s
Shear wave speed	c_s	3299 m/s
Shear modulus	μ	36 GPa
Thermal diffusivity	α_{th}	10^{-6} m ² /s
Specific heat	ρc	2.7 MPa/K
Shear zone half-width	w	10 mm
Rate-and-state parameters		
Reference slip velocity	V_*	10^{-6} m/s
Reference friction coefficient	f_*	0.6
Rate-and-state direct effect (VW)	a	0.010
Rate-and-state evolution effect (VW)	b	0.015
Rate-and-state evolution effect (VS)	b	0.003
Length scales		
Fault length	λ	96 km
Frictional domain	λ_{fr}	72 km
Velocity-weakening region	λ_{VW}	24 km
Cell size	Δz	3.3 m
Quasi-static cohesive zone	Λ_0	84 m
Nucleation size (Rice & Ruina, 1983)	h_{RR}^*	226 m
Nucleation size (Rubin & Ampuero, 2005)	h_{RA}^*	550 m

Table 1. Model parameters used in all simulations unless otherwise specified.

Parameter	Symbol	TP 1	TP 2	TP 3	TP 4
Interseismic effective normal stress (MPa)	$\bar{\sigma} = (\sigma - p_{int})$	25	25	25	50
Rate-and-state direct effect (VS)	a	0.050	0.050	0.025	0.050
Characteristic slip (mm)	L	1	1	1	2
Coupling coefficient (MPa/K)	Λ	0.1	0.34	0.34	0.34
Hydraulic diffusivity m ² /s	α_{hy}	10^{-3}	10^{-3}	10^{-4}	10^{-3}

Table 2. Parameters for models including thermal pressurization of pore fluids.

Parameter	Symbol	RS 1	RS 2
Interseismic effective normal stress (MPa)	$\bar{\sigma} = (\sigma - p_{int})$	20	10
Rate-and-state direct effect (VS)	a	0.050	0.050
Characteristic slip (mm)	L	1	0.5
Quasi-static cohesive zone (m)	Λ_0	106	106
Nucleation size (m), Rice & Ruina, 1983	h_{RR}^*	282	282
Nucleation size (m), Rubin & Ampuero, 2005	h_{RA}^*	688	688

Table 3. Parameters for models including only standard rate-and-state friction.

801 **Acknowledgments**

802 This study was supported by the National Science Foundation (grants EAR 1724686)
 803 and the Southern California Earthquake Center (SCEC), contribution No. 10782. SCEC
 804 is funded by NSF Cooperative Agreement EAR-1033462 and USGS Cooperative Agree-
 805 ment G12AC20038. D. Faulkner was supported by the Natural Environment Research
 806 Council (grants NE/P002943/1 and NE/R017484/1). The numerical simulations for this
 807 work were done on the High Performance Computing Central cluster of the California
 808 Institute of Technology. The data supporting the analysis and conclusions is given in Fig-
 809 ures and Tables, in the main text and supplementary materials. Data is accessible through
 810 the CaltechDATA repository (<https://data.caltech.edu/records/1612>). We thank Tom
 811 Heaton, Hiroo Kanamori, and Emily Brodsky for helpful discussions.

812 **References**

- 813 Acosta, M., Passelègue, F. X., Schubnel, A., & Violay, M. (2018). Dynamic weaken-
 814 ing during earthquakes controlled by fluid thermodynamics. *Nature Communi-*
 815 *cations*, *9*(1), 3074. doi: 10.1038/s41467-018-05603-9
- 816 Ader, T. J., Lapusta, N., Avouac, J.-P., & Ampuero, J.-P. (2014, 05). Response of
 817 rate-and-state seismogenic faults to harmonic shear-stress perturbations. *Geo-*
 818 *physical Journal International*, *198*(1), 385-413. Retrieved from [https://doi](https://doi.org/10.1093/gji/ggu144)
 819 [.org/10.1093/gji/ggu144](https://doi.org/10.1093/gji/ggu144) doi: 10.1093/gji/ggu144
- 820 Allmann, B. P., & Shearer, P. M. (2009). Global variations of stress drop for mod-
 821 erate to large earthquakes. *Journal of Geophysical Research: Solid Earth*,
 822 *114*(B1). doi: 10.1029/2008JB005821
- 823 Bandis, S., Lumsden, A., & Barton, N. (1981). Experimental studies of scale effects
 824 on the shear behaviour of rock joints. *International Journal of Rock Mechanics*
 825 *and Mining Sciences & Geomechanics Abstracts*, *18*(1), 1 - 21. doi: [https://doi](https://doi.org/10.1016/0148-9062(81)90262-X)
 826 [.org/10.1016/0148-9062\(81\)90262-X](https://doi.org/10.1016/0148-9062(81)90262-X)
- 827 Bangs, N., Moore, G., Gulick, S., Pangborn, E., Tobin, H., Kuramoto, S., & Taira,

- 828 A. (2009). Broad, weak regions of the Nankai Megathrust and implications for
829 shallow coseismic slip. *Earth and Planetary Science Letters*, *284*(1), 44 - 49.
- 830 Ben-David, O., Cohen, G., & Fineberg, J. (2010). The dynamics of the onset of fric-
831 tional slip. *Science*, *330*(6001), 211–214. doi: 10.1126/science.1194777
- 832 Bhattacharya, P., Rubin, A. M., & Beeler, N. M. (2017). Does fault strengthening
833 in laboratory rock friction experiments really depend primarily upon time and
834 not slip? *Journal of Geophysical Research: Solid Earth*, *122*(8), 6389-6430.
835 doi: <https://doi.org/10.1002/2017JB013936>
- 836 Bouchon, M., & Karabulut, H. (2008). The aftershock signature of supershear earth-
837 quakes. *Science*, *320*(5881), 1323–1325. doi: 10.1126/science.1155030
- 838 Brodsky, E. E., Kirkpatrick, J. D., & Candela, T. (2016, 01). Constraints from fault
839 roughness on the scale-dependent strength of rocks. *Geology*, *44*(1), 19-22. doi:
840 10.1130/G37206.1
- 841 Brown, K., Kopf, A., Underwood, M., & Weinberger, J. (2003). Compositional and
842 fluid pressure controls on the state of stress on the Nankai subduction thrust:
843 A weak plate boundary. *Earth and Planetary Science Letters*, *214*(3), 589 -
844 603.
- 845 Brune, J. N., Henyey, T. L., & Roy, R. F. (1969). Heat flow, stress, and rate of
846 slip along the San Andreas Fault, California. *Journal of Geophysical Research*,
847 *74*(15), 3821-3827.
- 848 Byerlee, J. (1978). Friction of rocks. *Pure and Applied Geophysics*, *116*(4-5), 615-
849 626. doi: 10.1007/BF00876528
- 850 Cattania, C. (2019). Complex earthquake sequences on simple faults. *Geophysical*
851 *Research Letters*, *46*(17-18), 10384-10393. doi: 10.1029/2019GL083628
- 852 Chen, J., Verberne, B. A., & Spiers, C. J. (2015a). Effects of healing on the seis-
853 mogenic potential of carbonate fault rocks: Experiments on samples from the
854 longmenshan fault, sichuan, china. *Journal of Geophysical Research: Solid*
855 *Earth*, *120*(8), 5479-5506. doi: <https://doi.org/10.1002/2015JB012051>

- 856 Chen, J., Verberne, B. A., & Spiers, C. J. (2015b). Interseismic re-strengthening
857 and stabilization of carbonate faults by "non-dieterich" healing under hy-
858 drothermal conditions. *Earth and Planetary Science Letters*, *423*, 1 - 12. doi:
859 <https://doi.org/10.1016/j.epsl.2015.03.044>
- 860 Collettini, C., Niemeijer, A., Viti, C., & Marone, C. (2009). Fault zone fabric and
861 fault weakness. *Nature*, *462*(7275), 907–910. doi: 10.1038/nature08585
- 862 De Paola, N., Holdsworth, R. E., Viti, C., Collettini, C., & Bullock, R. (2015).
863 Can grain size sensitive flow lubricate faults during the initial stages of earth-
864 quake propagation? *Earth and Planetary Science Letters*, *431*, 48 - 58. doi:
865 <https://doi.org/10.1016/j.epsl.2015.09.002>
- 866 Di Toro, G., Han, R., Hirose, T., De Paola, N., Nielsen, S., Mizoguchi, K., ... Shi-
867 mamoto, T. (2011, mar). Fault lubrication during earthquakes. *Nature*, *471*,
868 494.
- 869 Dieterich, J. H. (1979). Modeling of rock friction 1. experimental results and consti-
870 tutive equations. *Journal of Geophysical Research*, *84*(B5), 2161-2168.
- 871 Dieterich, J. H., & Kilgore, B. D. (1994). Direct observation of frictional contacts:
872 New insights for state-dependent properties. *Pure and Applied Geophysics*,
873 *143*, 283?302. doi: 10.1007/BF00874332
- 874 Dunham, E. M., Belanger, D., Cong, L., & Kozdon, J. E. (2011, 10). Earthquake
875 Ruptures with Strongly Rate-Weakening Friction and Off-Fault Plasticity,
876 Part1: Planar Faults. *Bulletin of the Seismological Society of America*, *101*(5),
877 2296-2307. doi: 10.1785/0120100075
- 878 Fang, Z., & Dunham, E. M. (2013). Additional shear resistance from fault rough-
879 ness and stress levels on geometrically complex faults. *Journal of Geophysical*
880 *Research: Solid Earth*, *118*(7), 3642-3654. doi: 10.1002/jgrb.50262
- 881 Faulkner, D. R., Mitchell, T. M., Behnsen, J., Hirose, T., & Shimamoto, T. (2011).
882 Stuck in the mud? earthquake nucleation and propagation through accre-
883 tionary forearcs. *Geophysical Research Letters*, *38*(18). doi: <https://doi.org/>

884 10.1029/2011GL048552

885 Faulkner, D. R., Mitchell, T. M., Healy, D., & Heap, M. J. (2006). Slip on 'weak'
 886 faults by the rotation of regional stress in the fracture damage zone. *Nature*,
 887 *444*(7121), 922–925. doi: 10.1038/nature05353

888 Field, E., Biasi, G., Bird, P., Dawson, T., Felzer, K.R., . . . Zeng, Y. (2013).
 889 Uniform California Earthquake Rupture Forecast, version 3 (UCERF3)
 890 –the time-independent model. *U.S. Geological Survey Open-File Report*
 891 *2013?1165, 97 p., California Geological Survey Special Report 228.* doi:
 892 <http://pubs.usgs.gov/of/2013/1165/>

893 Field, E. H., Jordan, T. H., Page, M. T., Milner, K. R., Shaw, B. E., Dawson, T. E.,
 894 . . . Thatcher, W. R. (2017). A synoptic view of the third Uniform California
 895 Earthquake Rupture Forecast (UCERF3). *Seismological Research Letters*,
 896 *88*(5), 1259–1267. doi: 10.1785/0220170045

897 Fineberg, J., & Bouchbinder, E. (2015). Recent developments in dynamic frac-
 898 ture: some perspectives. *International Journal of Fracture*, *196*(1), 33–57. Re-
 899 trieved from <https://doi.org/10.1007/s10704-015-0038-x> doi: 10.1007/
 900 s10704-015-0038-x

901 Freund, L. B. (1990). *Dynamic fracture mechanics*. Cambridge University Press. doi:
 902 10.1017/CBO9780511546761

903 Fukuyama, E., & Mizoguchi, K. (2010). Constitutive parameters for earthquake rup-
 904 ture dynamics based on high-velocity friction tests with variable sliprate. *In-*
 905 *ternational Journal of Fracture*, *163*(1), 15–26. doi: 10.1007/s10704-009-9417
 906 -5

907 Fulton, P. M., Brodsky, E. E., Kano, Y., Mori, J., Chester, F., Ishikawa, T., . . .
 908 Toczko, S. a. (2013). Low coseismic friction on the Tohoku-Oki fault deter-
 909 mined from temperature measurements. *Science*, *342*(6163), 1214–1217. doi:
 910 10.1126/science.1243641

911 Gabriel, A.-A., Ampuero, J.-P., Dalguer, L. A., & Mai, P. M. (2012). The tran-

- 912 sition of dynamic rupture styles in elastic media under velocity-weakening
913 friction. *Journal of Geophysical Research: Solid Earth*, 117(B9). doi:
914 10.1029/2012JB009468
- 915 Gao, X., & Wang, K. (2014). Strength of stick-slip and creeping subduction megathrusts
916 from heat flow observations. *Science*, 345(6200), 1038–1041. doi: 10
917 .1126/science.1255487
- 918 Goldsby, D. L., & Tullis, T. E. (2011). Flash heating leads to low frictional strength
919 of crustal rocks at earthquake slip rates. *Science*, 334(6053), 216–218. doi: 10
920 .1126/science.1207902
- 921 Greer, J. R., Oliver, W. C., & Nix, W. D. (2005). Size dependence of mechanical
922 properties of gold at the micron scale in the absence of strain gradients. *Acta
923 Materialia*, 53(6), 1821 - 1830. doi: <https://doi.org/10.1016/j.actamat.2004.12>
924 .031
- 925 Gu, J.-C., Rice, J. R., Ruina, A. L., & Tse, S. T. (1984). Slip motion and stability
926 of a single degree of freedom elastic system with rate and state dependent friction.
927 *Journal of the Mechanics and Physics of Solids*, 32(3), 167 - 196. doi:
928 [https://doi.org/10.1016/0022-5096\(84\)90007-3](https://doi.org/10.1016/0022-5096(84)90007-3)
- 929 Han, R., Shimamoto, T., Ando, J.-i., & Ree, J.-H. (2007). Seismic slip record in
930 carbonate-bearing fault zones: An insight from high-velocity friction experiments
931 on siderite gouge. *Geology*, 35(12), 1131-1134.
- 932 Hardebeck, J. L. (2015). Stress orientations in subduction zones and the strength of
933 subduction megathrust faults. *Science*, 349(6253), 1213–1216. doi: 10.1126/
934 science.aac5625
- 935 Hardebeck, J. L., & Hauksson, E. (1999). Role of fluids in faulting inferred from
936 stress field signatures. *Science*, 285(5425), 236–239. doi: 10.1126/science.285
937 .5425.236
- 938 Hardebeck, J. L., & Hauksson, E. (2001). Crustal stress field in southern cali-
939 fornia and its implications for fault mechanics. *Journal of Geophysical Re-*

- 940 *search: Solid Earth, 106*(B10), 21859-21882. doi: [https://doi.org/10.1029/](https://doi.org/10.1029/2001JB000292)
941 2001JB000292
- 942 Hauksson, E., Yang, W., & Shearer, P. M. (2012). Waveform Relocated Earthquake
943 Catalog for Southern California (1981 to June 2011). *Bulletin of the Seismolog-*
944 *ical Society of America, 102*(5), 2239-2244. doi: 10.1785/0120120010
- 945 Heaton, T. H. (1990). Evidence for and implications of self-healing pulses of slip
946 in earthquake rupture. *Physics of the Earth and Planetary Interiors, 64*(1), 1-
947 20.
- 948 Henye, T. L., & Wasserburg, G. J. (1971). Heat flow near major strike-slip faults
949 in California. *Journal of Geophysical Research (1896-1977), 76*(32), 7924-7946.
950 doi: 10.1029/JB076i032p07924
- 951 Ikari, M. J., Marone, C., & Saffer, D. M. (2011, 01). On the relation between fault
952 strength and frictional stability. *Geology, 39*(1), 83-86. doi: 10.1130/G31416
953 .1
- 954 Ishibe, T., & Shimazaki, K. (2012). Characteristic Earthquake Model and Seismicity
955 around Late Quaternary Archive Faults in Japan. *Bulletin of the Seismological*
956 *Society of America, 102*(3), 1041-1058. doi: 10.1785/0120100250
- 957 Jaeger, J., & Cook, N. (1976). *Fundamentals of rock mechanics*. London: Chapman
958 and Hall.
- 959 Jiang, J., & Lapusta, N. (2016). Deeper penetration of large earthquakes on seis-
960 mically quiescent faults. *Science, 352*(6291), 1293–1297. doi: 10.1126/science
961 .aaf1496
- 962 Kagan, Y. Y., Jackson, D. D., & Geller, R. J. (2012). Characteristic Earthquake
963 Model, 1884–2011, RIP. *Seismological Research Letters, 83*(6), 951-953. doi:
964 10.1785/0220120107
- 965 Kaneko, Y., & Lapusta, N. (2008). Variability of earthquake nucleation in con-
966 tinuum models of rate-and-state faults and implications for aftershock rates.
967 *Journal of Geophysical Research, 113*, B12312. doi: 10.1029/2007JB005154

- 968 Lachenbruch, A. H., & Sass, J. H. (1980). Heat flow and energetics of the San An-
 969 dreas Fault Zone. *Journal of Geophysical Research: Solid Earth*, *85*(B11),
 970 6185-6222. doi: 10.1029/JB085iB11p06185
- 971 Lambert, V., & Lapusta, N. (2020). Rupture-dependent breakdown energy in fault
 972 models with thermo-hydro-mechanical processes. *Solid Earth*, *11*(6), 2283–
 973 2302. doi: 10.5194/se-11-2283-2020
- 974 Lambert, V., Lapusta, N., & Perry, S. (in press). Propagation of large earthquakes
 975 as self-healing pulses and mild cracks. *Nature*.
- 976 Lapusta, N., Rice, J. R., Ben-Zion, Y., & Zheng, G. (2000). Elastodynamic analysis
 977 for slow tectonic loading with spontaneous rupture episodes on faults with
 978 rate- and state- dependent friction. *Journal of Geophysical Research*, *105*,
 979 765-789. doi: 10.1029/2000JB900250
- 980 Lockner, D. A., Morrow, C., Moore, D., & Hickman, S. (2011). Low strength of deep
 981 San Andreas fault gouge from SAFOD core. *Nature*, *472*(7341), 82–85. doi: 10
 982 .1038/nature09927
- 983 Lu, X., Rosakis, A. J., & Lapusta, N. (2010). Rupture modes in laboratory earth-
 984 quakes: Effect of fault prestress and nucleation conditions. *Journal of Geophys-
 985 ical Research: Solid Earth*, *115*(B12). doi: 10.1029/2009JB006833
- 986 Marone, C. (1998). Laboratory-derived friction laws and their application to seismic
 987 faulting. *Annual Review of Earth and Planetary Sciences*, *26*(1), 643-696. doi:
 988 10.1146/annurev.earth.26.1.643
- 989 McLaskey, G. C., Kilgore, B. D., Lockner, D. A., & Beeler, N. M. (2014). Lab-
 990 oratory generated m -6 earthquakes. *Pure and Applied Geophysics*, *171*(10),
 991 2601–2615. doi: 10.1007/s00024-013-0772-9
- 992 Michailos, K., Smith, E. G., Chamberlain, C. J., Savage, M. K., & Townend, J.
 993 (2019). Variations in seismogenic thickness along the Central Alpine Fault,
 994 New Zealand, revealed by a decade’s relocated microseismicity. *Geochemistry,
 995 Geophysics, Geosystems*, *20*(1), 470-486. doi: 10.1029/2018GC007743

- 1096 Michel, S., Avouac, J.-P., Lapusta, N., & Jiang, J. (2017). Pulse-like partial ruptures
1097 and high-frequency radiation at creeping-locked transition during megath-
1098 rust earthquakes. *Geophysical Research Letters*, *44*(16), 8345-8351. doi:
1099 10.1002/2017GL074725
- 1000 Nankali, H. R. (2011). Slip rate of the Kazerun Fault and Main Recent Fault (Za-
1001 gros, Iran) from 3D mechanical modeling. *Journal of Asian Earth Sciences*,
1002 *41*, 89-98. doi: 10.1016/j.jseaes.2010.12.009
- 1003 Nielsen, S., Spagnuolo, E., Violay, M., Smith, S., Di Toro, G., & Bistacchi, A.
1004 (2016). G: Fracture energy, friction and dissipation in earthquakes. *Jour-
1005 nal of Seismology*, *20*(4), 1187–1205. doi: 10.1007/s10950-016-9560-1
- 1006 Noda, H., Dunham, E. M., & Rice, J. R. (2009). Earthquake ruptures with
1007 thermal weakening and the operation of major faults at low overall stress
1008 levels. *Journal of Geophysical Research: Solid Earth*, *114*(B7). doi:
1009 10.1029/2008JB006143
- 1010 Noda, H., & Lapusta, N. (2010). Three-dimensional earthquake sequence simulations
1011 with evolving temperature and pore pressure due to shear heating: Effect of
1012 heterogeneous hydraulic diffusivity. *Journal of Geophysical Research*, *115*,
1013 B123414. doi: 10.1029/2010JB007780
- 1014 Noda, H., & Lapusta, N. (2012). On averaging interface response during dynamic
1015 rupture and energy partitioning diagrams for earthquakes. *Journal of Applied
1016 Mechanics*, *79*. doi: 10.1115/1.4005964
- 1017 Noda, H., Lapusta, N., & Kanamori, H. (2013). Comparison of average stress
1018 drop measures for ruptures with heterogeneous stress change and impli-
1019 cations for earthquake physics. *Geophysical Journal International*. doi:
1020 10.1093/gji/ggt074
- 1021 Page, M. T., & Felzer, K. (2015). Southern San Andreas Fault seismicity is
1022 consistent with the Gutenberg-Richter magnitude-frequency distribution.
1023 *Bulletin of the Seismological Society of America*, *105*(4), 2070-2080. doi:

1024 10.1785/0120140340

1025 Page, M. T., & van der Elst, N. J. (2018). Fault-tolerant b-values and aftershock
1026 productivity. *Journal of Geophysical Research: Solid Earth*, *123*(12), 10,880-
1027 10,888. doi: <https://doi.org/10.1029/2018JB016445>

1028 Perry, S. M., Lambert, V., & Lapusta, N. (2020). Nearly magnitude-invariant stress
1029 drops in simulated crack-like earthquake sequences on rate-and-state faults
1030 with thermal pressurization of pore fluids. *Journal of Geophysical Research:*
1031 *Solid Earth*. doi: 10.1029/2019JB018597

1032 Pharr, G. M., Herbert, E. G., & Gao, Y. (2010). The indentation size effect:
1033 A critical examination of experimental observations and mechanistic in-
1034 terpretations. *Annual Review of Materials Research*, *40*(1), 271-292. doi:
1035 10.1146/annurev-matsci-070909-104456

1036 Rice, J. R. (2006). Heating and weakening of faults during earthquake slip. *Journal*
1037 *of Geophysical Research*, *111*, B05311. doi: 10.1029/2005JB004006

1038 Rice, J. R., & Ruina, A. L. (1983). Stability of steady frictional slipping. *Journal of*
1039 *Applied Mechanics*, *50*(2), 343-349.

1040 Rubin, A., & Ampuero, J.-P. (2005). Earthquake nucleation on (aging) rate and
1041 state faults. *Journal of Geophysical Research: Solid Earth*, *110*(B11).

1042 Rubino, V., Rosakis, A. J., & Lapusta, N. (2017). Understanding dynamic friction
1043 through spontaneously evolving laboratory earthquakes. *Nature Communica-*
1044 *tions*, *8*(1), 15991. doi: 10.1038/ncomms15991

1045 Rubinstein, S. M., Cohen, G., & Fineberg, J. (2004). Detachment fronts
1046 and the onset of dynamic friction. *Nature*, *430*(7003), 1005–1009. doi:
1047 10.1038/nature02830

1048 Rubinstein, S. M., Cohen, G., & Fineberg, J. (2006, Jun). Contact area measure-
1049 ments reveal loading-history dependence of static friction. *Phys. Rev. Lett.*, *96*,
1050 256103. doi: 10.1103/PhysRevLett.96.256103

1051 Ruina, A. (1983). Slip instability and state variable friction laws. *Journal of Geo-*

- 1052 *physical Research*, 88(B12), 10359-10370.
- 1053 Schwartz, D. P., & Coppersmith, K. J. (1984). Fault behavior and characteristic
1054 earthquakes— examples from the wasatch and san andreas fault zones. *Journal*
1055 *of Geophysical Research*, 89, 5681-5698.
- 1056 Segall, P., & Rice, J. R. (2006). Does shear heating of pore fluid contribute to earth-
1057 quake nucleation? *Journal of Geophysical Research: Solid Earth*, 111(B9). doi:
1058 10.1029/2005JB004129
- 1059 Sibson, R. H. (1973). Interactions between temperature and pore-fluid pressure dur-
1060 ing earthquake faulting and a mechanism for partial or total stress relief. *Na-*
1061 *ture*, 243(126), 66-68.
- 1062 Sibson, R. H. (1975). Generation of pseudotachylyte by ancient seismic faulting.
1063 *Geophysical Journal of the Royal Astronomical Society*, 43(3), 775-794. doi: 10
1064 .1111/j.1365-246X.1975.tb06195.x
- 1065 Sieh, K. E. (1978, 12). Central California foreshocks of the great 1857 earthquake.
1066 *Bulletin of the Seismological Society of America*, 68(6), 1731-1749.
- 1067 Simons, M., Minson, S. E., Sladen, A., Ortega, F., Jiang, J., Owen, S. E., ... Webb,
1068 F. H. (2011). The 2011 magnitude 9.0 tohoku-oki earthquake: Mosaicking the
1069 megathrust from seconds to centuries. *Science*, 332(6036), 1421-1425. doi:
1070 10.1126/science.1206731
- 1071 Sone, H., & Shimamoto, T. (2009). Frictional resistance of faults during accelerat-
1072 ing and decelerating earthquake slip. *Nature Geoscience*, 2(10), 705-708. doi:
1073 10.1038/ngeo637
- 1074 Suppe, J. (2007, 12). Absolute fault and crustal strength from wedge tapers. *Geol-*
1075 *ogy*, 35(12), 1127-1130. doi: 10.1130/G24053A.1
- 1076 Svetlizky, I., & Fineberg, J. (2014). Classical shear cracks drive the onset of dry fric-
1077 tional motion. *Nature*, 509(7499), 205-208. doi: 10.1038/nature13202
- 1078 Tanikawa, W., & Shimamoto, T. (2009). Frictional and transport properties of the
1079 chelungpu fault from shallow borehole data and their correlation with seis-

- mic behavior during the 1999 Chi-Chi earthquake. *Journal of Geophysical Research: Solid Earth*, *114*(B1). doi: 10.1029/2008JB005750
- Tenthorey, E., & Cox, S. F. (2006). Cohesive strengthening of fault zones during the interseismic period: An experimental study. *Journal of Geophysical Research: Solid Earth*, *111*(B9). doi: <https://doi.org/10.1029/2005JB004122>
- Thom, C. A., Brodsky, E. E., Carpick, R. W., Pharr, G. M., Oliver, W. C., & Goldsby, D. L. (2017). Nanoscale roughness of natural fault surfaces controlled by scale-dependent yield strength. *Geophysical Research Letters*, *44*(18), 9299-9307. doi: 10.1002/2017GL074663
- Tinti, E., Fukuyama, E., Piatanesi, A., & Cocco, M. (2005). A Kinematic Source-Time Function Compatible with Earthquake Dynamics. *Bulletin of the Seismological Society of America*, *95*(4), 1211-1223. doi: 10.1785/0120040177
- Tinti, E., Scognamiglio, L., Micheli, A., & Cocco, M. (2016). Slip heterogeneity and directivity of the ML 6.0, 2016, Amatrice earthquake estimated with rapid finite-fault inversion. *Geophysical Research Letters*, *43*(20).
- Tormann, T., Wiemer, S., & Mignan, A. (2014). Systematic survey of high-resolution b value imaging along californian faults: Inference on asperities. *Journal of Geophysical Research: Solid Earth*, *119*(3), 2029-2054. doi: <https://doi.org/10.1002/2013JB010867>
- Townend, J., & Zoback, M. D. (2000). How faulting keeps the crust strong. *Geology*, *28*(5), 399-402. doi: 10.1130/0091-7613(2000)28(399:HFKTCS)2.0.CO;2
- Townend, J., & Zoback, M. D. (2004). Regional tectonic stress near the San Andreas fault in central and Southern California. *Geophysical Research Letters*, *31*(15). doi: 10.1029/2003GL018918
- Tsutsumi, A., & Shimamoto, T. (1997). High-velocity frictional properties of gabbro. *Geophysical Research Letters*, *24*(6), 699-702. doi: 10.1029/97GL00503
- Uchic, M. D., Dimiduk, D. M., Florando, J. N., & Nix, W. D. (2004). Sample dimensions influence strength and crystal plasticity. *Science*, *305*(5686), 986-

- 1108 989. doi: 10.1126/science.1098993
- 1109 Wesnousky, S. G. (1994). The Gutenberg-Richter or characteristic earthquake dis-
1110 tribution, which is it? *Bulletin of the Seismological Society of America*, 84(6),
1111 1940-1959.
- 1112 Wibberley, C. A. J., Yielding, G., & Toro, G. D. (2008). Recent advances in the
1113 understanding of fault zone internal structure: a review. In *The Internal
1114 Structure of Fault Zones: Implications for Mechanical and Fluid-Flow Proper-
1115 ties*. Geological Society of London. doi: 10.1144/SP299.2
- 1116 Yamashita, F., Fukuyama, E., Mizoguchi, K., Takizawa, S., Xu, S., & Kawakata, H.
1117 (2015). Scale dependence of rock friction at high work rate. *Nature*, 528(7581),
1118 254–257. doi: 10.1038/nature16138
- 1119 Yasuhara, H., Marone, C., & Elsworth, D. (2005). Fault zone restrengthening
1120 and frictional healing: The role of pressure solution. *Journal of Geophysical
1121 Research: Solid Earth*, 110(B6). doi: <https://doi.org/10.1029/2004JB003327>
- 1122 Ye, L., Lay, T., Kanamori, H., & Rivera, L. (2016a). Rupture characteristics of
1123 major and great ($M_w > 7.0$) megathrust earthquakes from 1990 to 2015: 1.
1124 source parameter scaling relationships. *Journal of Geophysical Research: Solid
1125 Earth*, 121(2), 826-844. doi: 10.1002/2015JB012426
- 1126 Ye, L., Lay, T., Kanamori, H., & Rivera, L. (2016b). Rupture characteristics of ma-
1127 jor and great ($M_w > 7.0$) megathrust earthquakes from 1990 to 2015: 2. depth
1128 dependence. *Journal of Geophysical Research: Solid Earth*, 121(2), 845-863.
1129 doi: 10.1002/2015JB012427
- 1130 Zheng, G., & Rice, J. R. (1998). Conditions under which velocity-weakening friction
1131 allows a self-healing versus a crack-like mode of rupture. *Bulletin of the Seis-
1132 mological Society of America*, 88(6), 1466-1483.
- 1133 Zoback, M., Hickman, S., & Ellsworth, W. (2010). Scientific drilling into the San
1134 Andreas fault zone. *Eos, Transactions American Geophysical Union*, 91, 197-
1135 199. doi: 10.1029/2010EO220001